Ore Geology Reviews 122 (2020) 103512

Contents lists available at ScienceDirect

Ore Geology Reviews

journal homepage: www.elsevier.com/locate/oregeorev

# Pyrite textures and compositions in Jiangshan gold deposit, Bengbu Uplift, southeastern North China Craton: Implications for ore genesis

Yang Chen[a,b,c], Yu Fan[a,b,c,*], Tao-Fa Zhou[a,b,c], Bin Fu[d], Yi-Nan Liu[a,b,c], Biao Wang[a,b,c], Qing Liu[e]

[a] School of Resource and Environmental Engineering, Hefei University of Technology, Hefei 230009, Anhui, China
[b] Ore Deposit and Exploration Centre (ODEC), Hefei University of Technology, Hefei 230009, Anhui, China
[c] Anhui Province Engineering Research Center for Mineral Resources and Mine Environments, Hefei 230009, Anhui, China
[d] Research School of Earth Science, Australian National University, Canberra, Australian Capital Territory 0200, Australia
[e] No. 312 Unit of Geology and Mineral Exploration of Anhui Province, Bengbu, Anhui 233040, China

ARTICLE INFO

*Keywords:*
Jiangshan gold deposit
Pyrite trace element
In situ sulfur isotope
Fracture-disseminated type gold deposit

ABSTRACT

Many Phanerozoic gold deposits in East China, e.g., those in the Jiaodong Peninsula, hosted either in granitoids of the same age or Precambrian basement rocks of the North China Craton, have been well documented. The Bengbu Uplift along the southeastern margin of the North China Craton is believed to be the western extension of the Jiaodong gold province, separated by the large-scale sinistral Tan-Lu Fault Zone. However, no deposits with more than 10 t gold resources have been discovered in the Bengbu Uplift, and it is unclear whether the timing and genesis of gold deposits in the Bengbu Uplift are similar to those in the Jiaodong gold province.

In this study, laser ablation inductively coupled plasma mass spectrometry trace element analyses, mapping, and in situ sulfur isotope analyses were used to determine the source and process of gold mineralization in Jiangshan gold deposit, the largest in the region. The wall rocks in the Jiangshan gold deposit are metamorphic rocks of the Neo-Archaean Wuhe Group, and the ore bodies are controlled by the eastern part of the Guangou–Xiajijia Fault. Four stages were identified from cross-cutting relationships and textural and mineralogical characteristics: pre-ore stage (stage I), quartz–pyrite–muscovite alteration (stage II), pyrite–quartz veins (stage III), and quartz–pyrite veinlets (stage IV). Each of the four stages is characterized by a different type of pyrite, here named Py1, Py2, Py3 and Py4. Py1 formes the core of Py2, has elliptical and irregular shapes, contains low gold and arsenic concentrations, and has $\delta^{34}S$ values of 0.86–2.86‰. Py2 is hosted in quartz–-pyrite–muscovite-altered rocks with disseminated and aggregated euhedral to subhedral textures. It has elevated arsenic content and the lowest gold content, with some rhythmic zones and fractures. Stage II was crosscut by stage III. Py3 has anhedral textures with brittle deformation and occupies fractures in stage III pyrite–quartz veins. The gold content of Py3 is slightly higher than that of Py1 and Py2, but its arsenic content is extremely low. Py4 in the quartz–pyrite veinlets has cataclastic textures with the highest gold and chalcophile element contents. Native gold and electrum also formed in stage IV, which is the main gold stage in the Jiangshan deposit. The $\delta^{34}S$ values of Py2–Py4 are broadly similar (5.79–7.98‰), suggesting a common sulfur source. Based on previous studies and higher $\delta^{34}S$ values of hydrothermal pyrite, the fluid sulfur isotopes are interpreted to relate to degassing of the mantle wedge metasomatized by slab fluids during the westward subduction of the palaeo-Pacific plate beneath the North China Craton during the early Cretaceous. Based on the geological characteristics of the deposit, we classify the Jiangshan gold deposit as a Jiaodong fracture-disseminated-type gold deposit which occurs as disseminated veinlets and disseminated mineralization in wallrocks along fracture zones. Tectonic events may be the most important factor in gold mineralization in fracture-disseminated type gold deposits.

## 1. Introduction

The Jiaodong Peninsula, located in the northeast of the North China Craton (NCC) and east of the Tan-Lu Fault Zone (Fig. 1), is the most important gold-producing region in China, with gold reserves in excess of 4000 t (Yang et al., 2014; Deng and Wang, 2016; Deng et al., 2020; Yang and Santosh, 2020). The Jiaodong Peninsula contains three gold metallogenic belts: Zhaoyuan–Laizhou, Muping–Rushan, and Penglai-

* Corresponding author at: School of Resource and Environmental Engineering, Hefei University of Technology, Hefei 230009, Anhui, China.
*E-mail address:* fanyu@hfut.edu.cn (Y. Fan).

https://doi.org/10.1016/j.oregeorev.2020.103512
Received 30 June 2019; Received in revised form 26 March 2020; Accepted 31 March 2020
Available online 01 April 2020

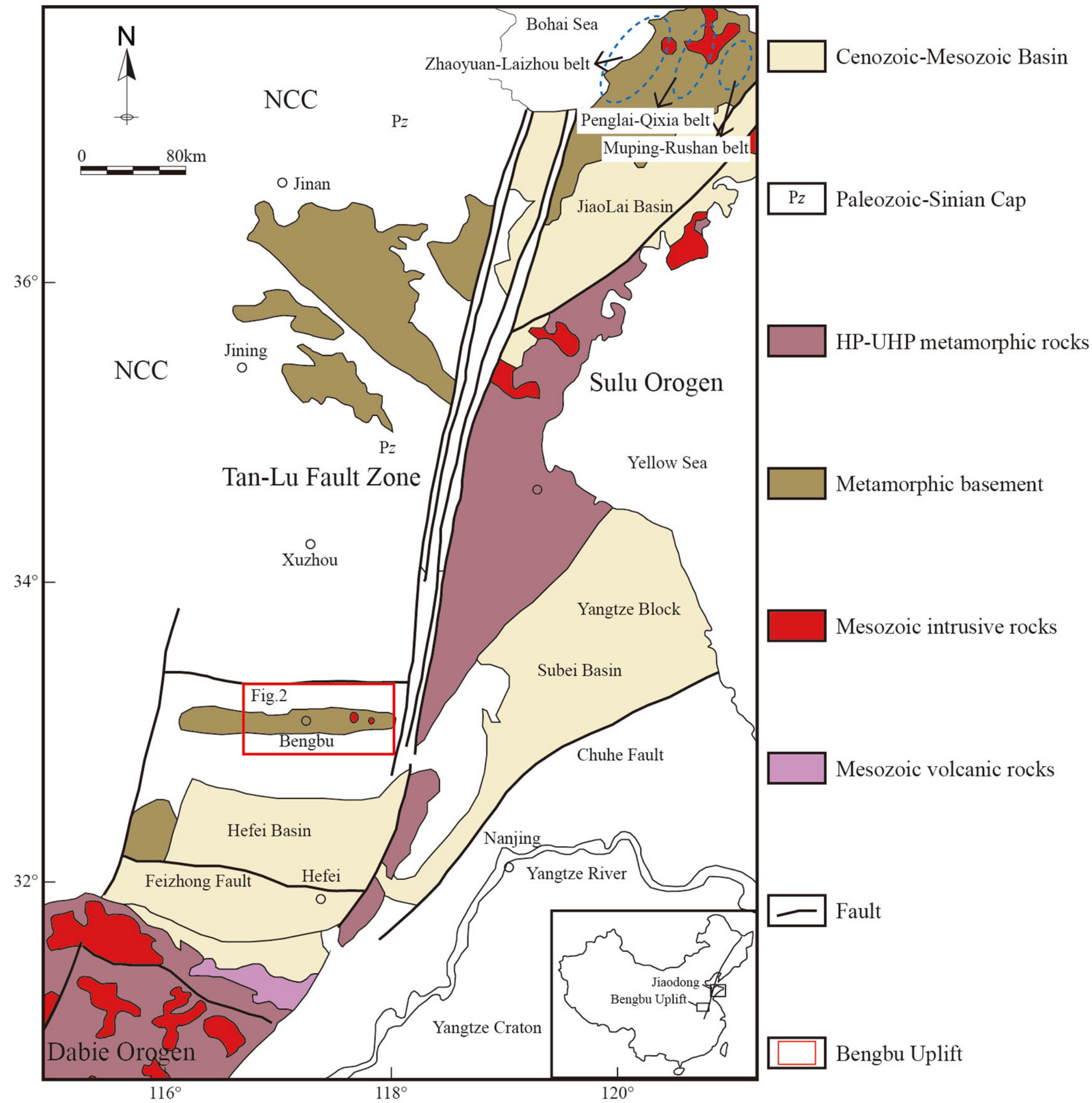


**Fig. 1.** Location map showing tectonic units (modified after Li et al., 2014).

Qixia (Yang et al., 2018); the Zhaoyuan-Laizhou belt contains more than 95% of the gold deposits (Yang and Santosh, 2015). Some researchers consider the Jiaodong gold deposits as “orogenic type” based on the character of mineralization (Goldgarb and Groves, 2015; Yang et al., 2016a; Groves and Santosh, 2016; Groves et al., 2020). Because of the nearly two billion year gap between the age of the regional metamorphic event and the gold mineralization, the deposits have also been classified as “Jiaodong type” (Li and Santosh, 2014; Deng and Wang, 2016; Deng et al., 2015, 2018, 2020; Yang and Santosh, 2020) and “Decratonic type” (Zhu et al., 2015; Cai et al., 2018).

The Bengbu Uplift in northern Anhui Province is located west of the Tan-Lu Fault Zone, and on the southeastern margin of the NCC (Fig. 1), adjacent to the Dabie–Sulu orogenic belt. This orogenic belt is offset by the large-scale sinistral strike-slip movement of the Tan-Lu Fault Zone (Xu et al., 1987; Zhu et al., 2005; Wang, 2006; Leech and Webb, 2013). Comprehensive comparative studies conducted on both sides of the Tan-Lu Fault Zone indicated that the Bengbu Uplift is the western extension of the Zhaoyuan–Laizhou gold belt (Zhu, 1999; Hu et al., 2015). Guo and Li (2009a) analysed the Palaeoproterozoic magmatism, metamorphic events, and geographical location of the Jiaodong Peninsula and Bengbu Uplift and suggested that the two regions were continuous prior to the movement of the Tan-Lu Fault Zone, which suggests that the Bengbu Uplift could potentially contain Jiaodong-type gold deposits (Zhai and Santosh, 2013; Li et al., 2015; Deng et al., 2015; Deng et al., 2018). However, only medium and small gold deposits have so far been found in the Bengbu Uplift, and the characteristics and ore-forming process of these gold deposits remain poorly studied.

The newly discovered Jiangshan deposit is the largest known gold deposit in the Bengbu Uplift, with reserves of about 20 t Au and an average gold grade of 2.41 g/t. Chen et al. (2018) studied the chronology of the host strata and related magmatic rocks in the Bengbu Uplift and determined the age of gold mineralization, but the ore-forming process and genesis of the deposit remain unclear. This study aimed to clarify the ore-forming process at Jiangshan, compare it with that of the Jiaodong gold deposits, and classify the deposit.

Pyrite is the dominant ore mineral in many types of gold deposit. Trace element concentrations and in situ sulfur isotopes in pyrite can indicate the character of the hydrothermal fluid responsible for the deposit, so these techniques have been widely used to determine the genesis of gold deposits (Large et al., 2007, 2009; Yang et al., 2016a; Hou et al., 2016; Ward et al., 2017; Li et al., 2018; Xiong et al., 2019). In Jiangshan gold deposit pyrite is the main gold-associated mineral

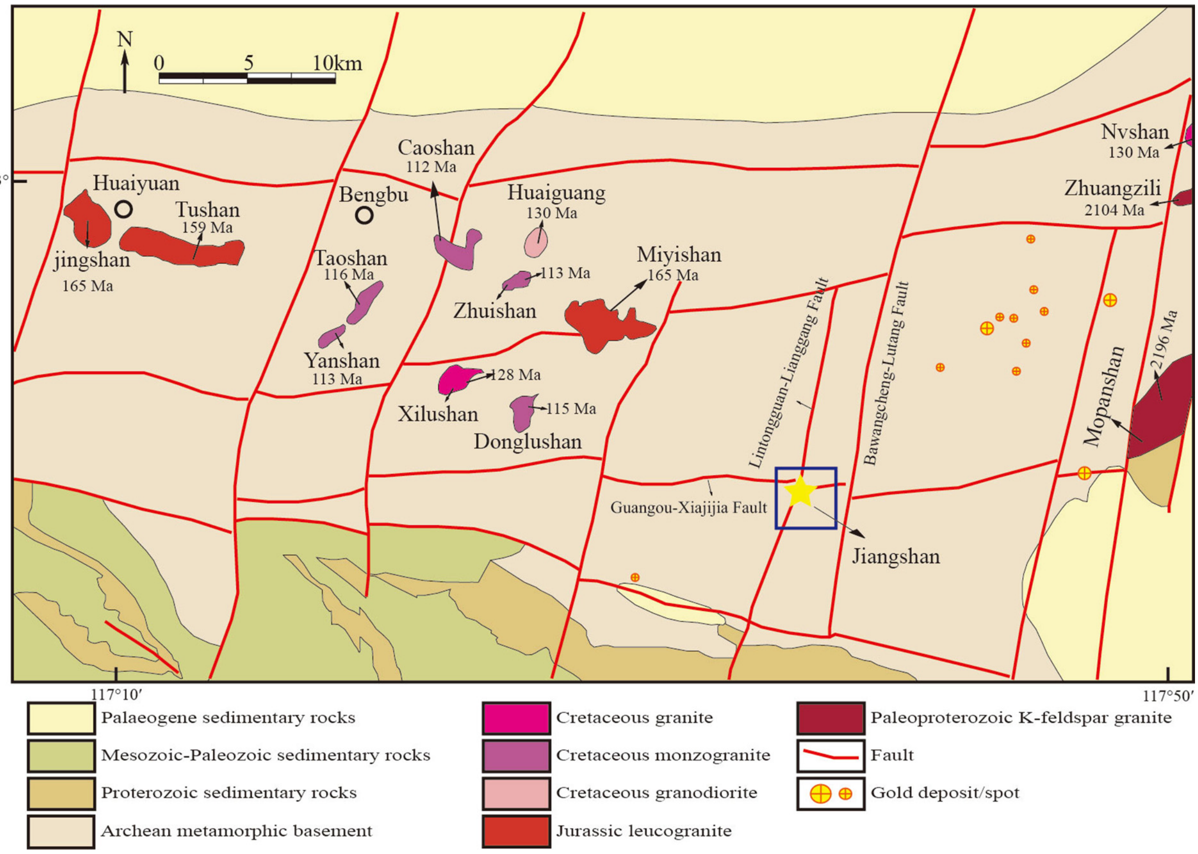


**Fig. 2.** Map of basement geology in the Bengbu uplift (modified after No. 312 Unit of Bureau of Geology and Mineral Exploration of Anhui Province).

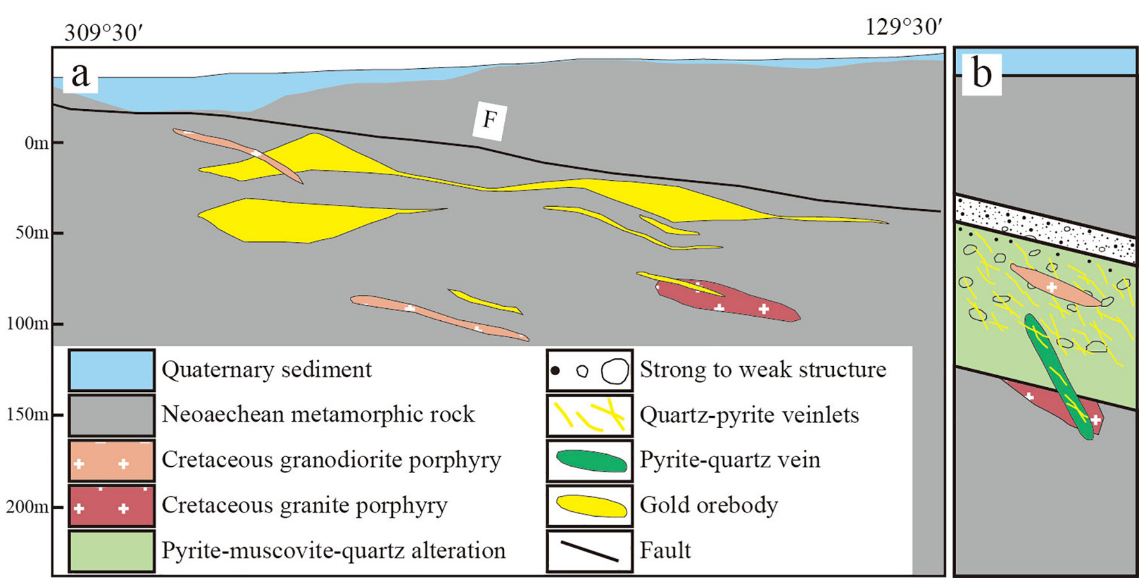


**Fig. 3.** Sketch map of ore body and fault zone in Jiangshan gold deposit, showing control of fault on mineralization. (a) No. 7 prospecting line profile of Jiangshan gold deposit (modified after No. 312 Unit of Bureau of Geology and Mineral Exploration of Anhui Province). (b) Sketch map of cross-cutting relationships between different rock types.

and was precipitated in each mineralization stage, making it suitable for study of deposit genesis.

In addition, this study aimed to clarify the detailed textures of pyrite in each mineralization stage of Jiangshan deposit and to divide them into different types. We then conducted compositional analyses of the different pyrites using laser ablation inductively coupled plasma mass spectrometry (LA-ICP-MS) and sensitive high-resolution ion microprobe (SHRIMP) analyses to reveal the trace element content and sulfur composition of each pyrite stage. The results provide insights into the source of sulfur, factors controlling mineralization, and evolution of the ore-forming fluid. Based on these results and those of previous studies, we discuss the process and mechanism of mineralization in fracture-disseminated-type gold deposits.

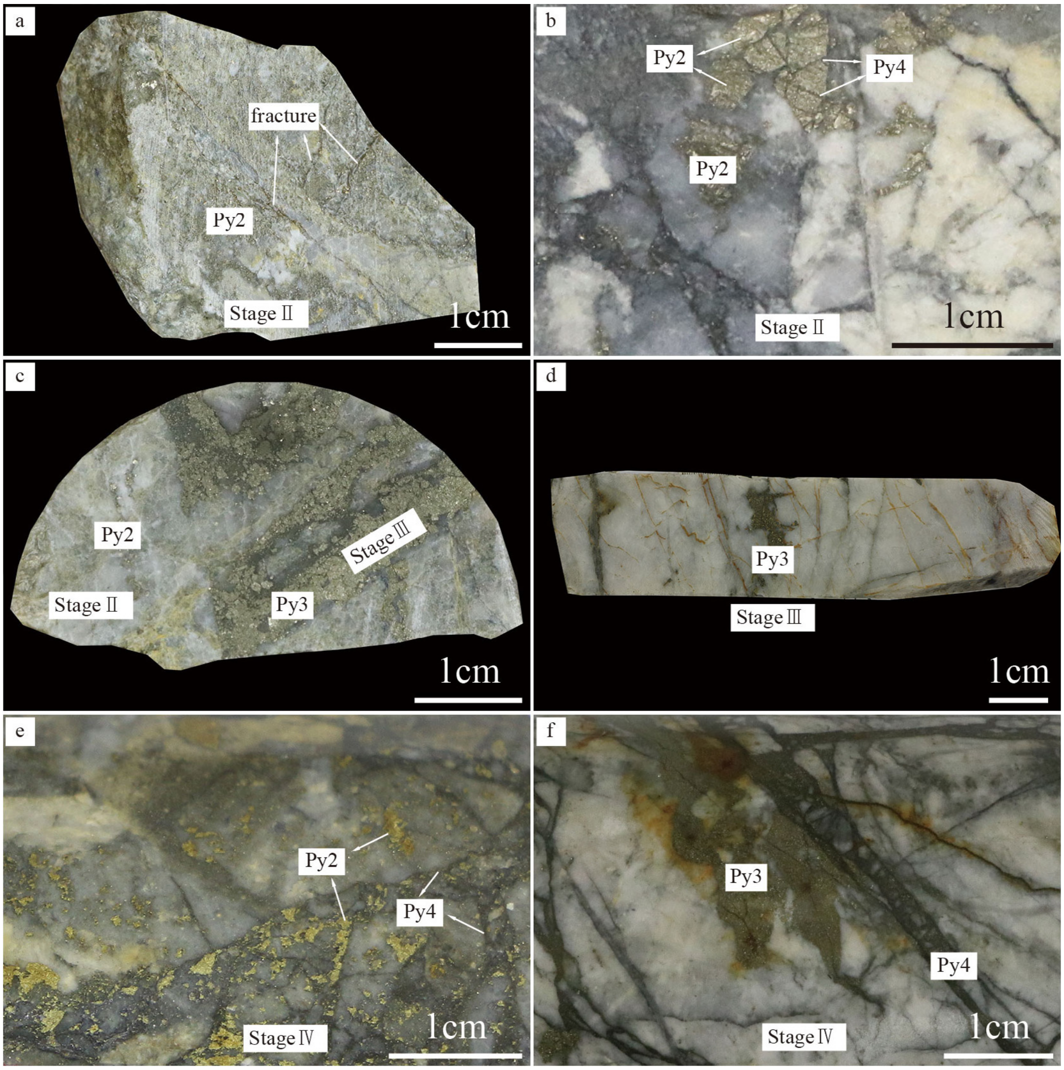


**Fig. 4.** Photographs of ore samples from Jiangshan gold deposit. (a) Fracture and Py2 occurs in pyrite–muscovite–quartz altered rocks. (b) Py4 cuts through Py2. (c) Pyrite–quartz vein cuts through pyrite–muscovite–quartz altered rock. (d) Py3 occurs as clusters in pyrite–quartz vein. (e) Py4 occurs as quartz–pyrite veinlet and cuts through Py2. (f) Py4 cuts through Py3.

## 2. Regional geology

The Bengbu Uplift, situated about 150 km north of the Dabie–Sulu orogenic belt, lies near the southeastern margin of the NCC, with the Hefei basin to its south and Tan-Lu Fault Zone to its east (Fig. 1). The exposed metamorphic basement of the Bengbu Uplift consists of Archaean Wuhe Group rocks (Fig. 2), which mainly comprise gneiss, amphibolite, marble, and supracrustal rocks. The Archaean metamorphic basement rocks in the Bengbu Uplift underwent granulite facies metamorphism during the Proterozoic (1.8–1.9 Ga), accompanied by synchronous magmatism, which is consistent with other Early Proterozoic complex belts in the NCC (Guo and Li, 2009b; Liu et al., 2012b). Proterozoic and Palaeozoic–Mesozoic sedimentary rocks developed in adjacent areas to the south and north (Fig. 1).

Mesozoic intrusions in the Bengbu Uplift have been traditionally divided into Late Jurassic and Early Cretaceous granitoids. The Late Jurassic Jingshan and Tushan granites intruded into the Wuhe complex at ~ 160 Ma, as indicated by zircon U–Pb dating (Xu et al., 2005; Yang et al., 2010; Li et al., 2014). Based on the low Mg–Fe content and scarcity of dark-coloured minerals in the Jingshan intrusion, Guo and Li (2009b) named it leucogranite. Early Cretaceous granitic intrusions, including granites, granodiorites, and monzongranites, were emplaced into the metamorphic basement at 130–110 Ma (Yang et al., 2005; Yang et al., 2010; Kang et al., 2018). Moreover, NNE-trending diabase, granite porphyry, diorite, and lamprophyre dikes cut across the Jingshan leucogranite and granodiorites (Liu et al., 2012a,b; Wu et al., 2015). No gold deposits have been found near or in the Mesozoic granitoids.

Structures in the Bengbu Uplift mainly comprise E- and NE- to NNE-trending faults (Fig. 2). The NE- to NNE-trending structures are thought to be subsidiary to the regional Tan-Lu Fault. The Jiangshan gold deposit is located at the junction of the E-trending Guangou–Xiajizhuang and NNE-trending Lintongguan–Lianggang Faults (Fig. 2).

## 3. Deposit geology

Jiangshan deposit was first explored in 2018. The deposit is covered by Quaternary sediments. Based on drill hole data, the wall rocks in this deposit are mainly Neo-Archaean Wuhe Group metamorphic rocks, including biotite–plagioclase gneiss, amphibolite, and leptite. The eastern part of the Guangou–Xiajijia Fault (F) occurs in Jiangshan deposit (Fig. 2), and ore zones are controlled by the fault, which generally trends SE, with a northward dip of about 35°. In the deposit, the fault is about 200 m long and 4–20 m wide.

There are no plutonic rocks in Jianshan deposit, but drill holes revealed two types of dike; pre-ore granite porphyry and post-ore

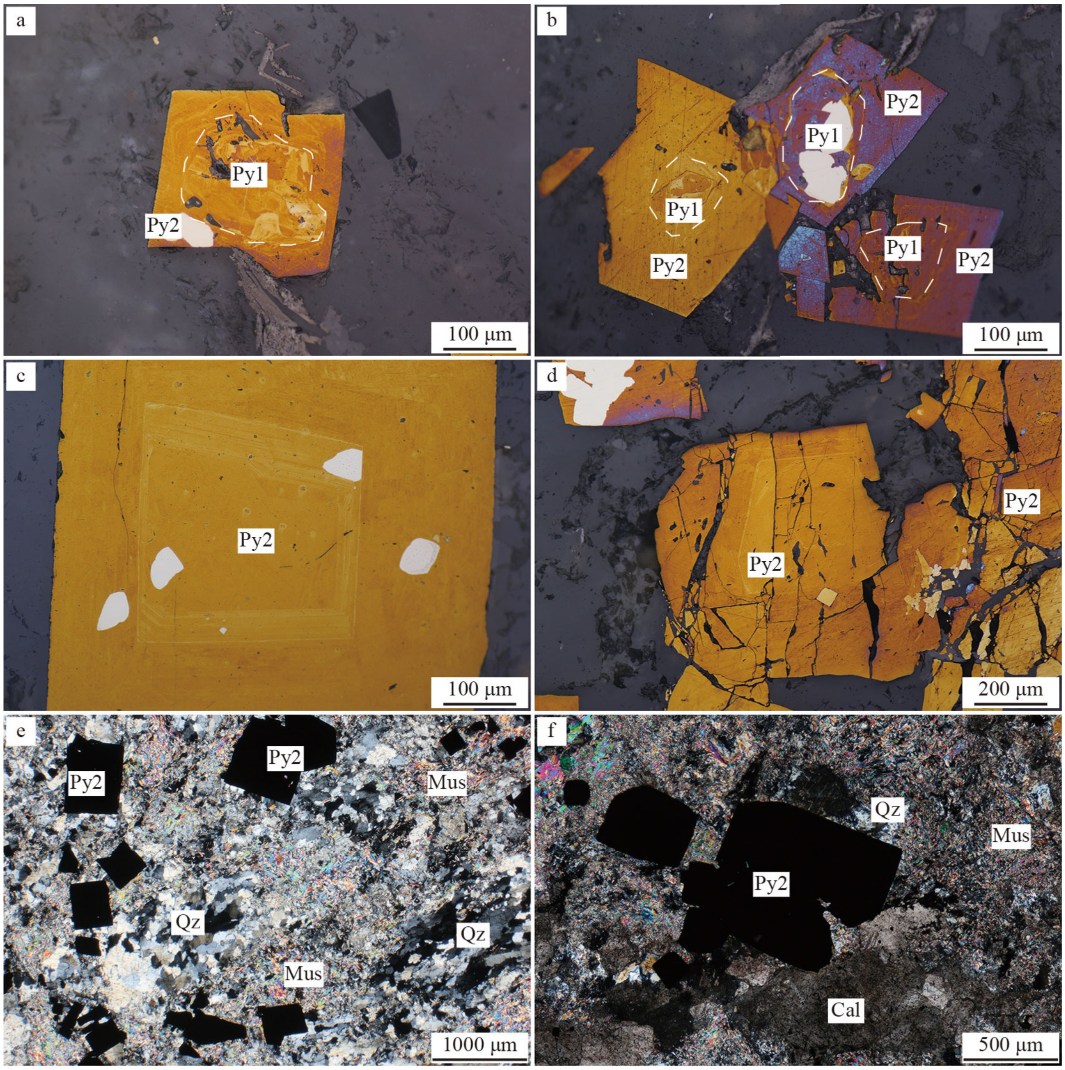


**Fig. 5.** Microphotographs and backscattered images of pyrite–muscovite–quartz altered rocks (a–d: photomicrographs of NaOCl-etched pyrites in reflected light; e–f: BSE images). (a, b) Py1 is overgrown by Py2. (c) Euhedral-zoned Py2. (d) Py2 with zones and fractures. (e) Quartz and muscovite coexisting with Py2. (f) Little carbonate alteration in pyrite-muscovite-quartz altered rocks. Py-pyrite; Qz-quartz; Mus-muscovite; Cal-carbonate.

**Table 1**
Summary of features of each types pyrite and the characterizing trace element trend.

| Stage | Type | Shape | Major | Minor |
|---|---|---|---|---|
| I | Py1 | Ellipse | Pb | Co, Ni |
| II | Py2 | Cube, pyritohedral | As | Au |
| III | Py3 | Planar | Co, Ni | As |
| IV | Py4 | Clastic, irregular | Au, Ag, As, Cu, Pb | Ni |

granodiorite porphyry (Fig. 3. Chen et al. (2018) reported that the ages of the two dikes are 128.3 ± 1.7 and 121.2 ± 1.4 Ma, respectively. Based on the relationship between mineralization and the dikes, the age of the gold mineralization was determined as 128–121 Ma (Chen et al., 2018). Over 50 gold ore bodies have been explored, and they all developed along the footwall fault plane (Fig. 3a). The ore bodies have a tabular shape and comprise fracture-altered rocks which occur as fracture texture and muscovite-quartz-pyrite alteration (Fig. 4a and 4b), pyrite–quartz veins (Fig. 4c and 4d), and quartz–pyrite veinlets (Fig. 4e and 4f). A large pyrite–muscovite–quartz-altered zone developed along the fault (Fig. 3b), and the alteration is cut by the pyrite–quartz veins (Fig. 4c) and quartz–pyrite veinlets (Fig. 4b and Fig. 4e). The fracture-altered rocks and quartz–pyrite veinlets are the dominant ore types in Jiangshan deposit.

Four stages of mineralization were noted in Jiangshan deposit. The first stage (Stage I) is the pre-ore stage, which formed the pre-ore stage pyrite (Py1) (Fig. 5a and 5b). Stage II is characterized by the formation of the pyrite–muscovite–quartz-altered zone. In this stage, the ore mineral is primarily pyrite, and the gangue minerals mainly consist of quartz, muscovite, and calcite (Fig. 5e and 5f). Pyrite occurs disseminated and as aggregates in altered rocks (Fig. 4a and 4b). Stage III comprises pyrite–quartz veins that cut through pyrite–quartz–muscovite-altered rocks (Fig. 4c); this stage is characterized by pyrite in quartz veins (Fig. 4d). Stage IV comprises quartz–pyrite veinlets that cut Stages II (Fig. 4b and 4e) and III (Fig. 4f).

## 4. Analytical methods

In situ trace element analyses and pyrite mapping were performed using LA-ICP-MS on polished thick sections at the In-situ Mineral Geochemistry Laboratory, Ore Deposit and Exploration Centre, Hefei University of Technology, China. The analyses were carried out on an Agilent 7900 Quadrupole ICP-MS coupled to a Photon Machines Analyte HE 193 nm ArF Excimer Laser Ablation System. A squid signal smoothing device was included in this laser ablation system. Helium was used as the carrier gas. Argon was used as the make-up gas and

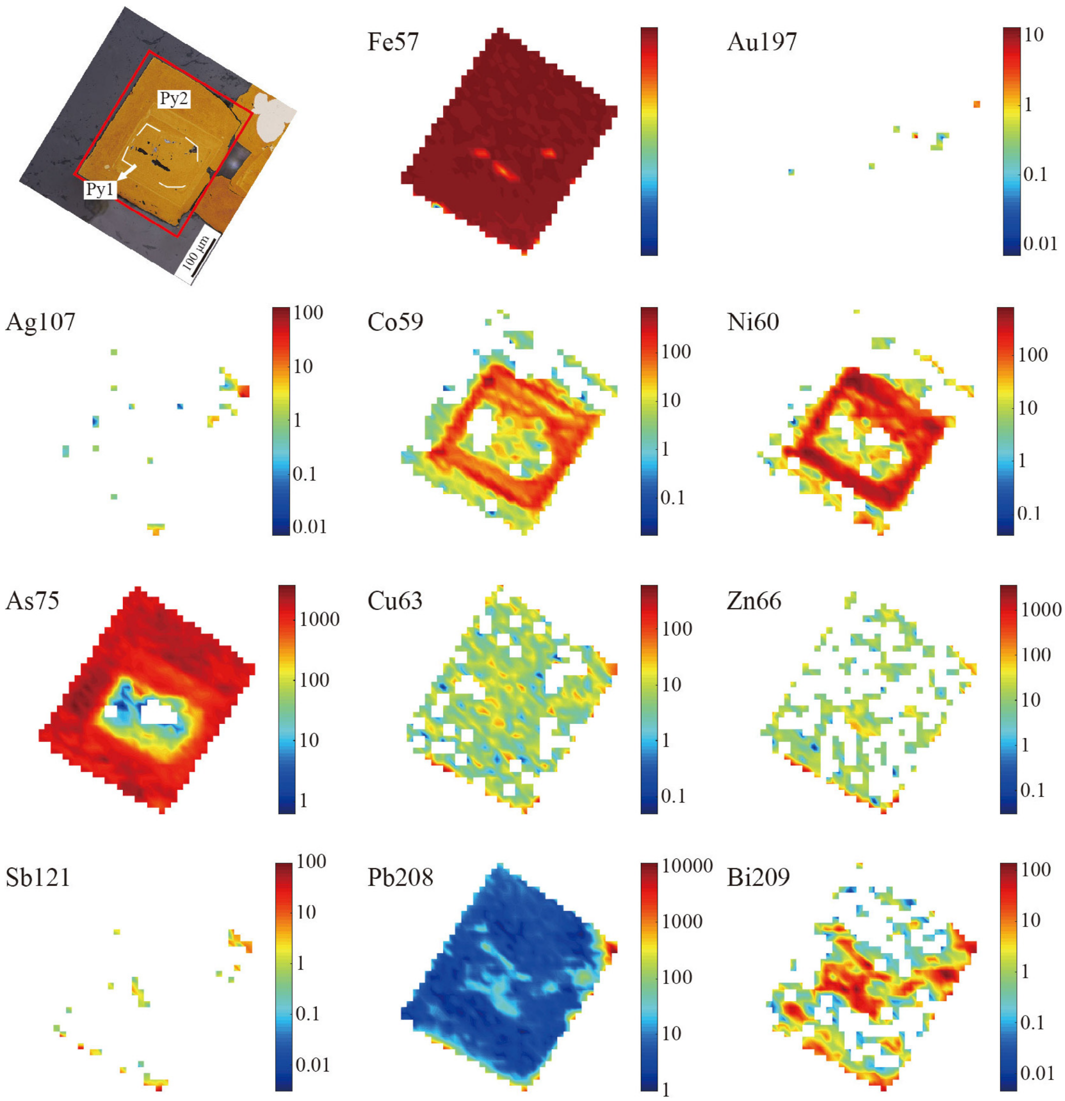


**Fig. 6.** Laser ablation inductively coupled plasma mass spectrometry images with logarithmic colour scales (in ppm) showing trace element contents of Py1 and Py2.

mixed with the carrier gas via a T-connector before entering the ICP (Ning et al., 2017; Wang et al., 2017). At the high He (0.9 l/min) and Ar (~0.9 l/min) flow rate, the cleaning efficiency is very high, the signal increases to top in less than 1 s, and washout time is less than 1.5 s. The element signals were smoothed during ablation. Each analysis was performed using a uniform spot diameter of 30 mm at 8 Hz with energy of ~ 4 J/cm$^2$ for 40 s after measuring the gas blank for 20 s. The following basic set of isotopes in pyrite was monitored: $^{23}$Na, $^{24}$Mg, $^{27}$Al, $^{29}$Si, $^{34}$S, $^{39}$K, $^{43}$Ca, $^{47}$Ti, $^{51}$V, $^{63}$Cr, $^{55}$Mn, $^{57}$Fe, $^{59}$Co, $^{60}$Ni, $^{65}$Cu, $^{66}$Zn, $^{75}$As, $^{77}$Se, $^{90}$Zr, $^{93}$Nb, $^{95}$Mo, $^{107}$Ag, $^{111}$Cd, $^{118}$Sn, $^{121}$Sb, $^{125}$Te, $^{157}$Gd, $^{178}$Hf, $^{181}$Ta, $^{182}$W, $^{197}$Au, $^{202}$Hg, $^{205}$Tl, $^{208}$Pb, and $^{209}$Bi. Standard reference materials GSE-1g, GSD-1g, BCR-2G and NIST 610 were used as external standards to plot calibration curve. The preferred values of element concentrations for the USGS reference glasses are from the GeoReM database (http://georem.mpch-mainz.gwdg.de/). Standard reference materials were run after each 10–15 unknowns; detection limits were calculated for each element in each spot analysis. The offline data processing was performed using a program called ICPMSDataCal (Liu et al., 2008). Trace element compositions of samples were calibrated against multiple reference materials with iron as the internal normalization element.

In situ sulfur isotope ($^{32}$S and $^{34}$S) analyses of pyrite from different stages were performed using Sensitive High-Resolution Ion MicroProbe – Stable Isotope (SHRIMP-SI) in the Research School of Earth Sciences, the Australian National University, Canberra (Ireland et al., 2014). Ruttan pyrite from Manitoba, Canada ($\delta^{34}S_{VCDT}$ = 1.2 ± 0.1‰. 2σ; Crow and Waughan, 1966) was used as the standard to calibrate all the data for unknowns. The average external reproducibility, as estimated from replicate measurements of the sulfur standard, was generally better than 0.58‰ (2σ) for the $\delta^{34}$S value.

## 5. Results

### 5.1. Pyrite texture

Various types of pyrite of different origins and showing different textures occur in Jiangshan deposit. NaOCl etching, detailed petrographic observations, and LA-ICP-MS mapping analyses were conducted on the pyrites. Based on the pyrite etched textures and crosscutting relationships, we divided the pyrites into four main types. The characteristics and major elements in each type are shown in Table 1.

- Py1: Pre-ore stage pyrite has an elliptical and irregular shape and diameter of 10–100 μm. Py1 contains silicate inclusions (Fig. 5a and 5b).
- Py2: This hydrothermal-stage pyrite occurs as euhedral and subhedral crystals disseminated and as aggregations in pyrite–quartz–muscovite-altered rocks. Py2 crystals vary from 50 to

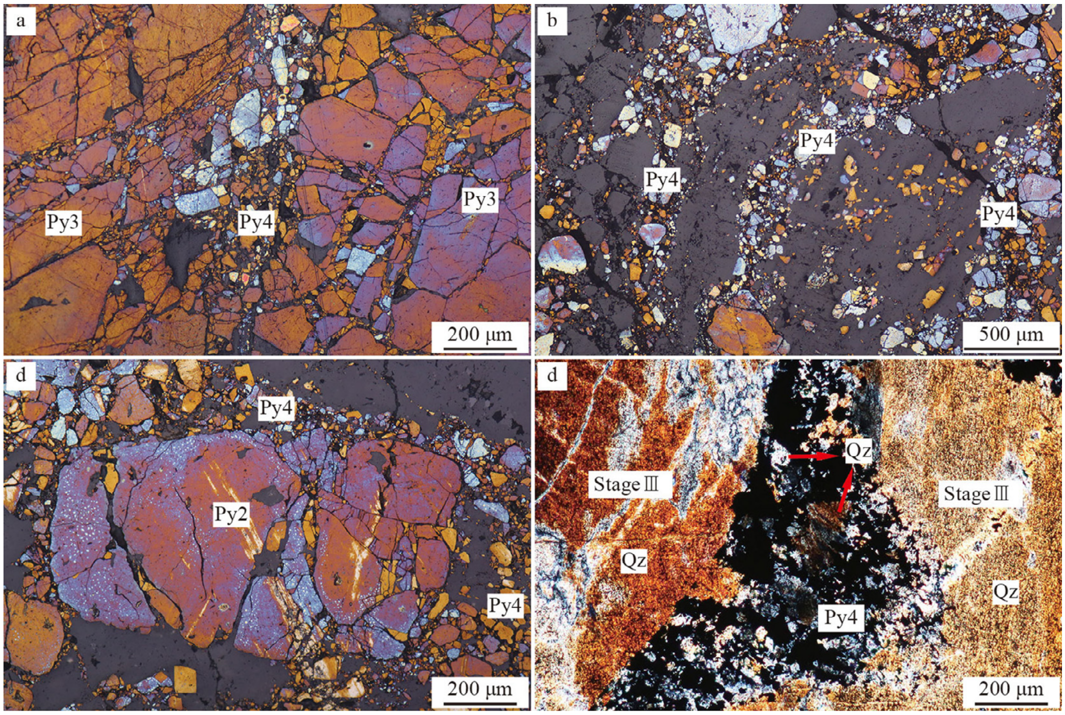


**Fig.7.** Photomicrographs of Py3 and Py4, and cross-cutting relationship of Py4 with Py2 and Py3. (a–c: photomicrographs of NaOCl-etched pyrites in reflected light. d: photomicrographs in transmitted light.) (a) Py3 with many fractures and Py4 in quartz–pyrite veinlet cross-cutting Py3. (b) Cataclastic texture of Py4 as veinlets. (c) Py4 cross-cutting Py2. (d) Quartz in quartz-pyrite shows cataclastic texture.

1000 µm in diameter. With NaOCl etching, some Py2 shows rhythmic zones (Fig. 5c); it commonly overgrows Py1. The boundary between Py1 and Py2 is irregular with corrosion textures (Fig. 5a and 5b). The LA-ICP-MS mapping showed differences between Py1 and Py2 (Fig. 6). Py2 shows strong deformation and fractures.

- Py3: This hydrothermal-stage pyrite occurs as clusters in pyrite–quartz veins (Fig. 4d). It has anhedral crystal forms, many fractures, and cataclastic textures (Fig. 7a). No zoning were found after NaOCl etching.
- Py4: This hydrothermal-stage pyrite has irregular shapes and cataclastic textures in quartz–pyrite veinlets (Fig. 7b). Py4 crystals vary from 5 to 100 µm and cut Py2 and Py3 (Fig. 7a and 7c). This type of pyrite is the last pyrite in Jiangshan deposit. 5.2 Pyrite trace element geochemistry.

A total of 71 LA-ICP-MS spot analyses were conducted, 14 on Py1, 20 on Py2, 15 on Py3, and 22 on Py4. The trace element data are shown in Table 2. Py1 has a gold content of 0.04–0.28 ppm (average = 0.18 ppm), silver content of 0.54–4.52 ppm (average = 2.01 ppm), cobalt content of 0.01–0.5 ppm (average = 0.1 ppm), and nickel content of 0.01–1.25 ppm (average = 0.27 ppm). The cobalt/nickel ratio varies between 0.1 and 10 (Fig. 8b). The arsenic content is relatively low, ranging from 40 to 218 ppm (average = 91 ppm). The trace element concentrations in Py2 are 0.01–0.33 ppm Au (average = 0.05 ppm), 0.01–1.44 ppm Ag (average = 0.34 ppm), 11.28–183.66 ppm Co (average = 57.13 ppm), 0.81–89.07 ppm Ni (average = 27.95 ppm), and 415.36–3072.60 ppm As (average = 1691.55 ppm). Most of the cobalt/nickel values are greater than 1 (Fig. 8b).

The trace element concentrations in Py3 are 0.09–2.31 ppm Au (average = 0.51 ppm), 0.21–2.05 ppm Ag (average = 0.74 ppm), 506.71–3061.48 Co ppm (average = 1432 ppm), 265.77–1689.03 ppm Ni (average = 653.71 ppm), and 1.04–90.53 ppm As (17.28 ppm). The cobalt/nickel values are greater than 1 (Fig. 8b). Py4 had the highest gold and silver contents (582 and 461 ppm, respectively), and an electrum nanoparticle was recognized. This data was only used in the gold–arsenic diagram. The trace element concentrations were 0.63–18.18 ppm Au (average = 2.65 ppm), 2.46–46.48 ppm Ag (average = 19.50 ppm), 10.32–200.32 ppm Co (average 79.56 ppm), 0.36–26.01 ppm Ni (average = 5.84 ppm), and 962.34–4814.88 ppm As (average = 2053.09 ppm). Most of the cobalt/nickel values are greater than 1 (Fig. 8b).

The cobalt and nickel contents in Py1 were the lowest, and the cobalt, nickel, and arsenic contents were relatively high compared to those of Py1 and Py3, but the gold content was the lowest. Py3 was cobalt- and nickel-rich, and its arsenic content was relatively low. Py4 had the highest gold content and was rich in chalcophile elements, such as arsenic, copper, antimony, and lead (Fig. 9c, 9d, 9g, and 9f). No positive correlation occurred between gold and arsenic in the four pyrite types (Fig. 8a). Cobalt and nickel had strong positive correlations (Fig. 8b); gold, silver, and copper were also positively correlated. The gold/silver values were less than 1.

### 5.2. In situ sulfur isotope composition of pyrite

All isotopic data (n = 32) for in situ sulfur isotopes analysed by SHRIMP are provided in Table 3. The $\delta^{34}S$ sulfur isotope values of Py1 were 0.86–2.86‰ (average = 1.89‰). The values of Py2, Py3, and Py4 were similar at 6.54–7.89‰ (average = 7.37‰, n = 13), 5.79–7.75‰ (average = 6.97‰, n = 9), and 6.35–7.54‰ (average = 7.07‰, n = 6), respectively. The core and edges showed different sulfur isotope values in Py2 than in the core of Py1 (Fig. 10a). The sulfur isotope values at different positions in Py2–Py4 were similar, ranging from 5 to 8‰ (Fig. 10b–10d).

## 6. Discussion

### 6.1. Gold occurrence and distribution

In most gold deposits, including those with visible or invisible gold, pyrite is the main gold-bearing mineral (Reich et al., 2005; Cook et al.,

**Table 2**
Selected LA-ICP-MS analyses of different pyrite types from the Jiangshan gold deposit. B.d.l (Below detection limit).

| Type | Ti49 | V51 | Cr53 | Mn55 | Co59 | Ni60 | Cu65 | Zn66 | As75 | Se77 | Mo95 | Ag107 | Sb121 | Au197 | Pb208 | Bi209 |
|---|---|---|---|---|---|---|---|---|---|---|---|---|---|---|---|---|
| Py1 | 0.90 | 0.02 | 0.34 | 0.37 | 0.01 | 0.07 | 6.97 | 0.44 | 52.99 | 2.22 | B.d.l | 0.54 | 0.48 | 0.10 | 23.07 | 4.06 |
| Py1 | 1.90 | 0.10 | 0.33 | 10.35 | 0.01 | 0.01 | 40.30 | 0.57 | 101.99 | 2.57 | 0.03 | 2.96 | 0.78 | 0.17 | 74.25 | 14.44 |
| Py1 | 2.24 | 0.02 | 0.75 | 0.35 | 0.13 | 0.41 | 47.98 | 0.94 | 47.13 | 2.08 | 0.25 | 2.04 | 0.59 | 0.22 | 55.02 | 11.21 |
| Py1 | 2.24 | 0.02 | 0.75 | 0.35 | 0.13 | 0.41 | 47.98 | 0.94 | 47.13 | 2.08 | 0.25 | 2.04 | 0.59 | 0.22 | 55.02 | 11.21 |
| Py1 | 1.90 | 0.01 | 0.16 | 0.45 | 0.01 | 0.16 | 18.48 | 0.81 | 40.69 | 3.14 | B.d.l | 1.11 | 0.45 | 0.16 | 23.20 | 4.41 |
| Py1 | 1.76 | 0.02 | 0.47 | 0.51 | 0.50 | 0.03 | 44.10 | 0.89 | 217.99 | 3.30 | B.d.l | 4.52 | 1.41 | 0.20 | 168.65 | 24.92 |
| Py1 | 2.55 | 0.03 | 0.33 | 0.42 | 0.01 | 0.03 | 7.07 | 0.36 | 49.68 | 4.57 | 0.07 | 3.66 | 0.16 | 0.20 | 15.99 | 21.56 |
| Py1 | 1.72 | 0.01 | 0.23 | 0.37 | 0.04 | 0.01 | 19.17 | 0.22 | 53.99 | 6.73 | 0.01 | 1.48 | 0.69 | 0.16 | 46.37 | 10.20 |
| Py1 | 1.73 | 0.02 | 8.23 | 0.39 | 0.01 | 0.02 | 18.11 | 0.58 | 190.97 | 3.42 | 0.01 | 2.01 | 1.24 | 0.28 | 50.17 | 11.44 |
| Py1 | 0.67 | 0.11 | 2.72 | 8.82 | 0.02 | 0.02 | 34.37 | 1.11 | 55.22 | 3.94 | 0.14 | 2.54 | 0.28 | 0.16 | 28.00 | 7.65 |
| Py1 | 0.87 | 0.04 | 0.16 | 0.44 | 0.12 | 0.24 | 9.58 | 0.32 | 94.20 | 3.79 | 0.10 | 1.30 | 0.82 | 0.25 | 41.07 | 12.82 |
| Py1 | 1.08 | 0.01 | 0.23 | 0.38 | 0.05 | 1.06 | 8.22 | 0.57 | 49.60 | 3.13 | 0.01 | 1.04 | 0.57 | 0.07 | 35.10 | 8.17 |
| Py1 | 1.07 | 0.02 | 4.34 | 0.44 | 0.13 | 1.25 | 16.71 | 0.69 | 77.56 | 3.06 | 0.07 | 1.82 | 1.12 | 0.25 | 69.37 | 14.25 |
| Py1 | 0.60 | 0.01 | 4.82 | 0.32 | 0.34 | 0.07 | 9.95 | 0.61 | 196.94 | 5.07 | 0.00 | 1.13 | 0.07 | 0.04 | 19.03 | 6.46 |
| Py2 | 3.80 | 0.01 | 0.15 | 0.35 | 36.59 | 50.68 | 0.30 | 0.23 | 1609.38 | 1.70 | 0.01 | 0.03 | 0.03 | 0.01 | 0.18 | 0.76 |
| Py2 | 22.34 | 0.03 | 0.40 | 0.45 | 36.66 | 58.56 | 0.3 | 0.17 | 415.36 | 2.02 | 0.01 | 0.03 | 0.05 | 0.02 | 0.37 | 1.14 |
| Py2 | 4.82 | 0.10 | 0.46 | 0.42 | 57.73 | 35.52 | 0.43 | 0.20 | 1323.59 | 1.62 | B.d.l | 0.79 | 0.09 | 0.01 | 6.47 | 16.62 |
| Py2 | 1.81 | 0.01 | 0.36 | 0.33 | 44.42 | 10.78 | 0.24 | 0.33 | 1500.95 | 3.67 | B.d.l | 0.01 | 0.03 | 0.03 | 0.10 | 0.08 |
| Py2 | 3.24 | 0.02 | 2.45 | 1.31 | 15.96 | 7.27 | 0.31 | 0.59 | 3072.60 | 6.51 | B.d.l | 0.04 | 0.05 | 0.13 | 0.21 | 0.85 |
| Py2 | 176.47 | 1.44 | 3.73 | 5.70 | 22.75 | 19.35 | 3.66 | 0.82 | 2147.32 | 3.73 | B.d.l | 0.96 | 0.88 | 0.04 | 37.97 | 11.44 |
| Py2 | 111.74 | 4.45 | 44.98 | 13.42 | 39.49 | 31.43 | 2.10 | 2.33 | 2197.93 | 5.85 | 0.01 | 0.32 | 0.67 | 0.03 | 11.62 | 20.28 |
| Py2 | 36.38 | 8.59 | 8.48 | 3.22 | 11.28 | 14.33 | 2.58 | 1.01 | 2447.49 | 7.98 | B.d.l | 0.17 | 0.80 | 0.03 | 22.58 | 37.05 |
| Py2 | 39.61 | 9.55 | 14.54 | 1.02 | 91.29 | 44.06 | 3.25 | 0.32 | 2026.05 | 3.76 | B.d.l | 1.44 | 2.45 | 0.33 | 22.71 | 20.38 |
| Py2 | 18.33 | 0.31 | 0.20 | 2.20 | 42.06 | 34.93 | 15.8 | 0.27 | 2690.30 | 7.51 | B.d.l | 0.92 | 3.45 | 0.23 | 46.96 | 6.36 |
| Py2 | 2.80 | 0.02 | 0.97 | 0.40 | 46.44 | 0.81 | 3.08 | 0.38 | 2088.23 | 6.73 | B.d.l | 0.25 | 0.06 | 0.03 | 3.97 | 0.61 |
| Py2 | 2.03 | 0.04 | 0.56 | 0.47 | 14.75 | 1.13 | 0.28 | 0.25 | 2114.06 | 5.84 | B.d.l | 0.01 | 0.05 | 0.01 | 0.41 | 0.15 |
| Py2 | 4.47 | 0.05 | 0.16 | 0.45 | 41.48 | 34.09 | 0.41 | 0.21 | 1879.08 | 5.20 | B.d.l | 0.06 | 0.04 | 0.01 | 0.94 | 1.13 |
| Py2 | 2.86 | 0.01 | 0.27 | 0.48 | 70.34 | 5.85 | 0.15 | 0.50 | 534.39 | 6.34 | 0.01 | 0.02 | 0.06 | 0.01 | 0.23 | 0.39 |
| Py2 | 7.63 | 0.88 | 0.97 | 1.71 | 27.49 | 6.48 | 0.29 | 0.62 | 651.28 | 5.66 | 0.01 | 0.13 | 0.02 | 0.01 | 1.06 | 4.86 |
| Py2 | 3.89 | 0.02 | 0.19 | 0.56 | 131.84 | 5.28 | 5.17 | 0.30 | 2337.91 | 4.95 | 0.01 | 0.14 | 1.22 | 0.02 | 12.34 | 0.70 |
| Py2 | 1.32 | 0.08 | 0.23 | 0.46 | 103.42 | 56.83 | 6.06 | 0.31 | 1002.21 | 8.97 | 0.01 | 0.60 | 1.16 | 0.05 | 16.43 | 18.91 |
| Py2 | 3.55 | 0.04 | 0.42 | 5.53 | 183.66 | 89.07 | 8.44 | 0.35 | 1489.96 | 5.34 | B.d.l | 0.64 | 0.81 | 0.05 | 22.90 | 8.32 |
| Py2 | 3.20 | 0.04 | 0.11 | 0.54 | 111.25 | 47.16 | 1.63 | 0.18 | 1055.96 | 7.14 | B.d.l | 0.05 | 0.22 | 0.02 | 2.32 | 1.37 |
| Py2 | 2.44 | 0.13 | 14.20 | 27.47 | 13.83 | 5.41 | 3.75 | 1.24 | 1246.85 | 4.96 | B.d.l | 0.08 | 0.65 | 0.02 | 13.12 | 2.47 |
| Py3 | 1.70 | 0.02 | 0.99 | 1.27 | 630.41 | 556.37 | 15.68 | 1.06 | 10.39 | 35.38 | 1.15 | 0.70 | 0.90 | 0.26 | 14.78 | 4.61 |
| Py3 | 729.78 | 6.55 | 14.94 | 0.33 | 506.71 | 265.77 | 2.62 | 0.30 | 90.53 | 14.93 | 0.01 | 0.41 | 0.47 | 0.09 | 12.51 | 20.45 |
| Py3 | 4.10 | 0.34 | 0.19 | 0.38 | 793.14 | 391.40 | 0.85 | 0.28 | 25.73 | 8.79 | 0.01 | 0.27 | 0.05 | 0.23 | 1.02 | 3.32 |
| Py3 | 6.12 | 0.17 | 0.10 | 0.34 | 2993.28 | 1582.52 | 1.79 | 0.31 | 38.60 | 18.90 | B.d.l | 0.21 | 0.04 | 0.13 | 0.55 | 4.07 |
| Py3 | 1.66 | 0.02 | 0.40 | 0.32 | 3061.48 | 344.02 | 6.19 | 0.53 | 20.71 | 14.48 | B.d.l | 1.95 | 0.49 | 1.09 | 7.85 | 2.57 |
| Py3 | 0.71 | 0.03 | 0.19 | 0.47 | 1541.17 | 641.36 | 2.43 | 0.41 | 17.22 | 18.50 | B.d.l | 2.05 | 0.03 | 2.31 | 3.14 | 0.92 |
| Py3 | 2.77 | 0.03 | 0.26 | 0.38 | 2974.92 | 191.63 | 1.36 | 0.51 | 15.13 | 20.75 | B.d.l | 0.39 | 0.07 | 0.51 | 3.62 | 1.21 |
| Py3 | 0.37 | 0.10 | 0.17 | 3.24 | 531.32 | 265.85 | 14.34 | 0.83 | 6.52 | 28.57 | 0.61 | 0.32 | 0.82 | 0.08 | 15.5 | 1.39 |
| Py3 | 1.27 | 0.10 | 0.61 | 1.69 | 1484.92 | 485.00 | 22.66 | 1.14 | 9.15 | 31.60 | 0.02 | 0.94 | 0.93 | 0.45 | 26.06 | 6.82 |
| Py3 | 2.02 | 0.02 | 0.09 | 0.45 | 1360.37 | 322.30 | 6.71 | 0.62 | 2.63 | 22.59 | 0.70 | 0.33 | 0.20 | 0.27 | 4.18 | 2.21 |
| Py3 | 3.33 | 0.01 | 0.31 | 0.37 | 949.82 | 801.87 | 6.00 | 0.62 | 1.71 | 36.53 | 0.91 | 0.22 | 0.10 | 0.23 | 1.57 | 2.73 |
| Py3 | 2.75 | 0.01 | 18.78 | 0.58 | 1983.18 | 1689.03 | 31.72 | 1.80 | 10.06 | 23.65 | 0.11 | 1.91 | 0.27 | 1.23 | 10.51 | 10.84 |
| Py3 | 2.98 | 0.02 | 0.23 | 0.48 | 1236.30 | 761.65 | 7.95 | 1.07 | 5.03 | 33.10 | 1.15 | 0.40 | 0.24 | 0.32 | 8.72 | 4.72 |
| Py3 | 2.79 | 0.01 | 0.17 | 0.53 | 540.88 | 208.74 | 3.17 | 0.62 | 1.04 | 39.51 | 0.24 | 0.63 | 0.11 | 0.19 | 2.68 | 0.97 |
| Py3 | 1.82 | 0.01 | 0.36 | 0.42 | 892.10 | 1298.08 | 6.11 | 0.80 | 4.68 | 27.12 | 0.53 | 0.33 | 0.20 | 0.19 | 3.43 | 4.09 |
| Py4 | 5.42 | 0.27 | 7.52 | 9.64 | 54.45 | 3.81 | 28.79 | 0.55 | 3225.05 | 3.11 | B.d.l | 2.46 | 0.77 | 0.63 | 73.38 | 15.12 |
| Py4 | 7.14 | 1.09 | 1.32 | 0.63 | 87.32 | 21.65 | 35.86 | 1.10 | 4814.88 | 4.64 | 0.01 | 24.51 | 5.29 | 1.35 | 467.41 | 108.29 |
| Py4 | 218.66 | 9.68 | 1.67 | 24.99 | 93.16 | 1.99 | 90.55 | 2.83 | 1206.03 | 7.38 | 0.33 | 17.68 | 7.57 | 1.33 | 112.07 | 41.79 |
| Py4 | 152.39 | 7.47 | 1.35 | 5.02 | 149.88 | 5.35 | 203.70 | 2.77 | 1745.23 | 9.87 | 0.41 | 25.9 | 5.08 | 1.97 | 117 | 87.84 |
| Py4 | 64.92 | 7.56 | 2.56 | 29.83 | 125.85 | 10.56 | 172.35 | 2.00 | 1735.72 | 6.11 | 0.29 | 30.63 | 6.12 | 2.51 | 131.17 | 95.78 |
| Py4 | 10.24 | 5.57 | 1.13 | 6.13 | 29.49 | 1.41 | 126.39 | 2.28 | 2153.72 | 8.13 | 0.27 | 21.15 | 4.01 | 1.77 | 84.39 | 71.77 |
| Py4 | 15.21 | 10.65 | 2.68 | 14.80 | 50.00 | 10.02 | 111.03 | 2.72 | 1327.43 | 8.24 | 0.36 | 20.36 | 6.07 | 1.73 | 86.64 | 62.88 |
| Py4 | 21.58 | 1.55 | 0.28 | 2.07 | 10.32 | 2.87 | 71.72 | 1.27 | 2003.49 | 5.59 | 0.25 | 16.13 | 4.14 | 2.06 | 107.21 | 74.62 |
| Py4 | 55.99 | 13.61 | 4.36 | 3.06 | 85.99 | 4.54 | 106.12 | 1.41 | 962.34 | 7.88 | 0.26 | 20.21 | 5.34 | 1.53 | 120.45 | 78.79 |
| Py4 | 1591.47 | 14.37 | 11.19 | 4.73 | 50.17 | 1.71 | 129.29 | 1.48 | 1948.03 | 8.59 | 0.26 | 24.12 | 4.39 | 1.96 | 83.94 | 73.60 |
| Py4 | 1.92 | 1.06 | 0.27 | 0.86 | 65.19 | 3.33 | 49.37 | 1.09 | 1619.60 | 9.11 | 0.01 | 20.47 | 1.88 | 7.22 | 48.24 | 59.09 |
| Py4 | 107.41 | 23.52 | 7.93 | 50.76 | 49.33 | 26.01 | 128.00 | 8.26 | 1388.83 | 15.97 | 0.01 | 24.07 | 6.76 | 1.29 | 240.65 | 152.37 |
| Py4 | 3.47 | 1.80 | 0.44 | 1.43 | 108.56 | 1.33 | 131.12 | 0.47 | 1996.00 | 7.61 | 0.07 | 30.92 | 3.60 | 3.24 | 133.77 | 61.91 |
| Py4 | 2.66 | 0.07 | 1.20 | 0.44 | 47.14 | 0.14 | 13.22 | 0.45 | 3408.34 | 4.16 | 0.01 | 4.12 | 0.93 | 0.75 | 43.28 | 42.73 |
| Py4 | 6.12 | 2.53 | 1.27 | 3.75 | 200.32 | 1.32 | 69.65 | 1.96 | 2381.24 | 8.79 | 0.20 | 14.58 | 3.79 | 0.87 | 155.45 | 52.74 |
| Py4 | 3.86 | 0.79 | 2.94 | 1.11 | 38.65 | 0.36 | 25.97 | 0.36 | 1497.18 | 4.22 | B.d.l | 7.65 | 1.15 | 0.64 | 76.12 | 47.25 |
| Py4 | 3.23 | 1.62 | 1.67 | 5.75 | 50.73 | 20.99 | 87.29 | 1.37 | 2503.70 | 6.24 | 0.23 | 23.51 | 5.46 | 1.60 | 99.10 | 47.49 |
| Py4 | 1.69 | 0.24 | 0.14 | 0.39 | 137.81 | 0.77 | 29.25 | 0.50 | 1699.44 | 6.48 | B.d.l | 8.46 | 1.78 | 1.18 | 75.24 | 38.45 |
| Py4 | 2.16 | 0.06 | 0.18 | 0.37 | 36.95 | 0.87 | 74.93 | 0.56 | 1076.68 | 3.72 | 0.03 | 19.32 | 1.92 | 2.65 | 109.9 | 80.34 |
| Py4 | 8.94 | 11.74 | 1.01 | 21.48 | 58.38 | 7.12 | 244.44 | 3.97 | 1541.09 | 11.32 | 0.19 | 46.48 | 10.98 | 18.18 | 197.01 | 195.87 |
| Py4 | 6.20 | 0.06 | 0.23 | 0.44 | 198.62 | 1.06 | 33.40 | 0.96 | 3345.93 | 3.98 | B.d.l | 6.71 | 1.14 | 1.12 | 71.25 | 43.73 |
| Py4 | 0.53 | 0.04 | 0.37 | 0.49 | 22.11 | 1.27 | 17.31 | 0.22 | 1588.18 | 4.33 | B.d.l | 461.29 | 1.00 | 582.29 | 68.17 | 23.20 |

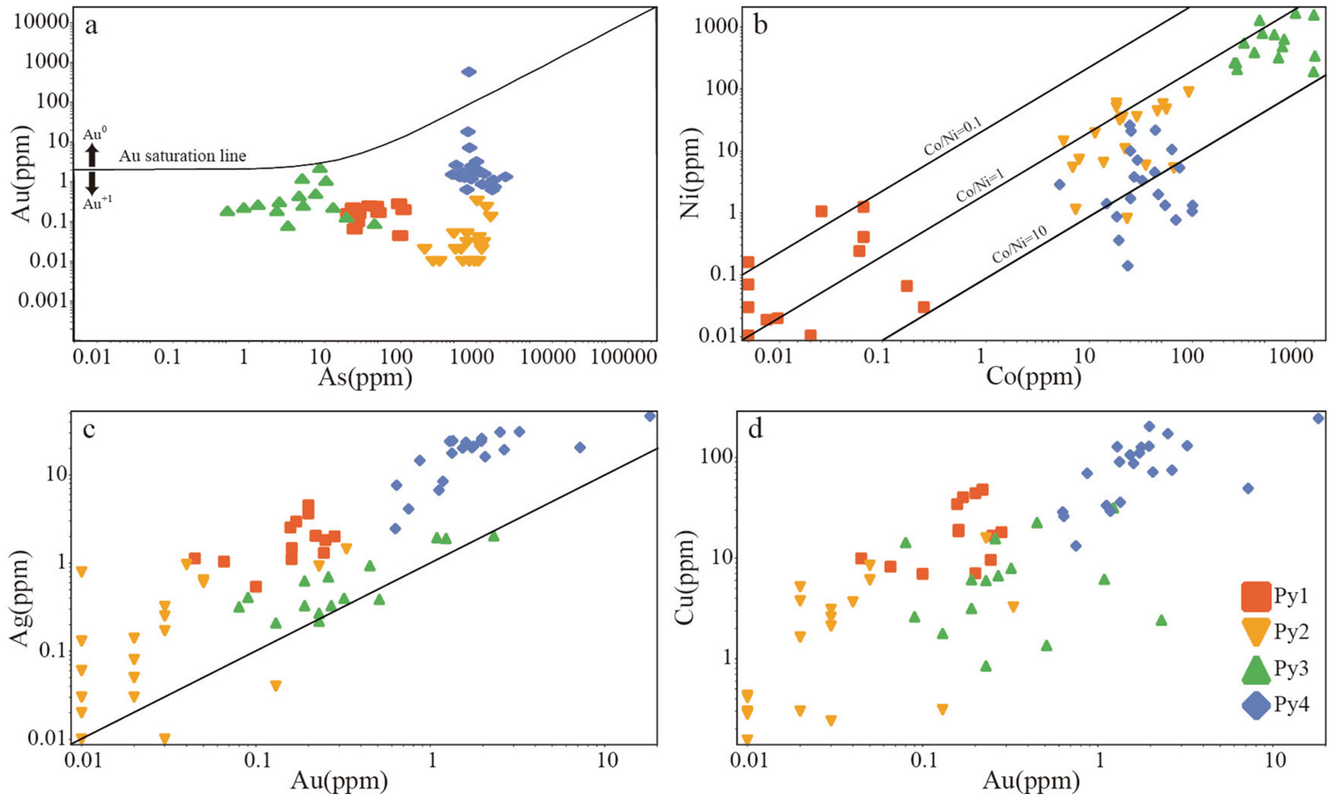


**Fig. 8.** Binary plots of selected trace elements. (a) Covariation of Au and As contents in pyrite; the dashed curve is the solubility limit of Au as a function of As, as determined by Reich et al. (2005). (b) The Co and Ni contents and Co/Ni ratios in pyrite. (c) Covariation of Au and Ag contents in pyrite. (d) Covariation of Au and Cu in pyrite.

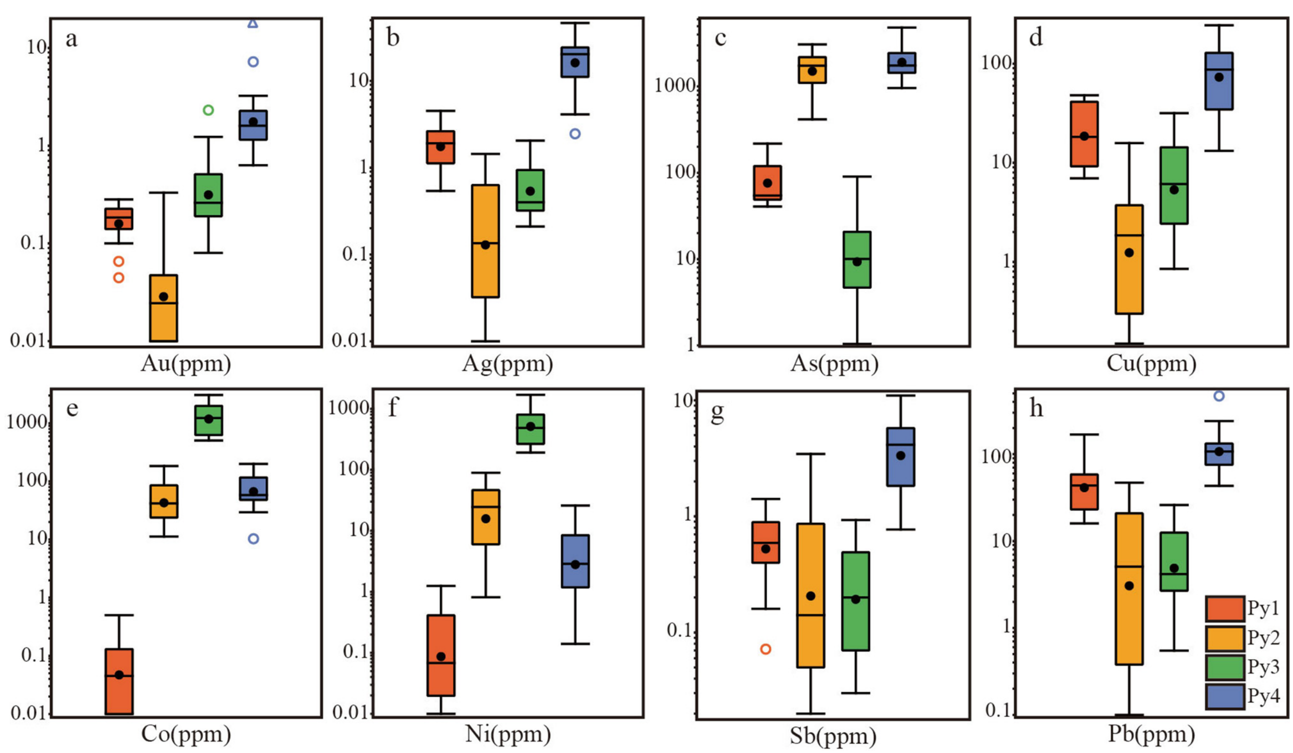


**Fig. 9.** Box and whisker plots of trace element concentrations for each pyrite types in the Jiangshan gold deposit (a Au. b Ag. c As. d Cu. e Co. f Ni. g Sb. h Pb). Whisker: min/max; thick line: median; black circles: mean; open circles and triangle: outlier threshold.

**Table 3**
SHRIMP sulfur isotopic composition (‰) of various types of pyrite in the Jiangshan gold deposit.

| Type | $^{32}S$ (CPS) | Raw $^{34}S/^{32}S$ Ratio | ± 2s | d$^{34}$S (‰, VCDT) | ± 2s (internal) | ± 2s (external) |
|---|---|---|---|---|---|---|
| Py1 | 6.72E+08 | 0.043680144 | 0.000008497 | 2.38 | 0.19 | 0.43 |
| Py1 | 5.79E+08 | 0.043639005 | 0.000018453 | 1.45 | 0.42 | 0.56 |
| Py1 | 6.57E+08 | 0.043701596 | 0.000010463 | 2.86 | 0.24 | 0.45 |
| Py1 | 6.52E+08 | 0.043613217 | 0.000023648 | 0.86 | 0.54 | 0.66 |
| Py2 | 6.15E+08 | 0.043903840 | 0.000007265 | 7.44 | 0.16 | 0.41 |
| Py2 | 6.53E+08 | 0.043891903 | 0.000006602 | 7.17 | 0.15 | 0.41 |
| Py2 | 6.54E+08 | 0.043864085 | 0.000014516 | 6.54 | 0.33 | 0.50 |
| Py2 | 6.47E+08 | 0.043889314 | 0.000006524 | 7.11 | 0.15 | 0.41 |
| Py2 | 6.69E+08 | 0.043887535 | 0.000009478 | 7.07 | 0.21 | 0.44 |
| Py2 | 6.54E+08 | 0.043897421 | 0.000012264 | 7.30 | 0.28 | 0.47 |
| Py2 | 7.65E+08 | 0.043900187 | 0.000010510 | 7.36 | 0.24 | 0.45 |
| Py2 | 6.53E+08 | 0.043917482 | 0.000010528 | 7.75 | 0.24 | 0.45 |
| Py2 | 6.61E+08 | 0.043906955 | 0.000016168 | 7.51 | 0.37 | 0.53 |
| Py2 | 6.79E+08 | 0.043913693 | 0.000013680 | 7.67 | 0.31 | 0.49 |
| Py2 | 6.85E+08 | 0.043927414 | 0.000007518 | 7.98 | 0.17 | 0.42 |
| Py2 | 5.72E+08 | 0.043907665 | 0.000012370 | 7.53 | 0.28 | 0.47 |
| Py2 | 6.47E+08 | 0.043898776 | 0.000011510 | 7.33 | 0.26 | 0.46 |
| Py3 | 8.04E+08 | 0.043830875 | 0.000008800 | 5.79 | 0.20 | 0.43 |
| Py3 | 7.89E+08 | 0.043890543 | 0.000021930 | 7.14 | 0.50 | 0.63 |
| Py3 | 8.17E+08 | 0.043837452 | 0.000012907 | 5.94 | 0.29 | 0.48 |
| Py3 | 8.32E+08 | 0.043917288 | 0.000011611 | 7.75 | 0.26 | 0.46 |
| Py3 | 7.92E+08 | 0.043907489 | 0.000008123 | 7.53 | 0.18 | 0.42 |
| Py3 | 6.70E+08 | 0.043912334 | 0.000011057 | 7.63 | 0.25 | 0.46 |
| Py3 | 7.85E+08 | 0.043891899 | 0.000011982 | 7.17 | 0.27 | 0.47 |
| Py3 | 7.70E+08 | 0.043883431 | 0.000010182 | 6.98 | 0.23 | 0.44 |
| Py3 | 7.88E+08 | 0.043875308 | 0.000007326 | 6.80 | 0.17 | 0.41 |
| Py4 | 7.65E+08 | 0.043900187 | 0.000010510 | 7.36 | 0.24 | 0.45 |
| Py4 | 7.72E+08 | 0.043879465 | 0.000006523 | 6.89 | 0.15 | 0.41 |
| Py4 | 8.11E+08 | 0.043855738 | 0.000019672 | 6.35 | 0.45 | 0.59 |
| Py4 | 8.03E+08 | 0.043908214 | 0.000009470 | 7.54 | 0.21 | 0.44 |
| Py4 | 6.55E+08 | 0.043900850 | 0.000008334 | 7.37 | 0.19 | 0.42 |
| Py4 | 7.83E+08 | 0.043881376 | 0.000012376 | 6.93 | 0.28 | 0.47 |

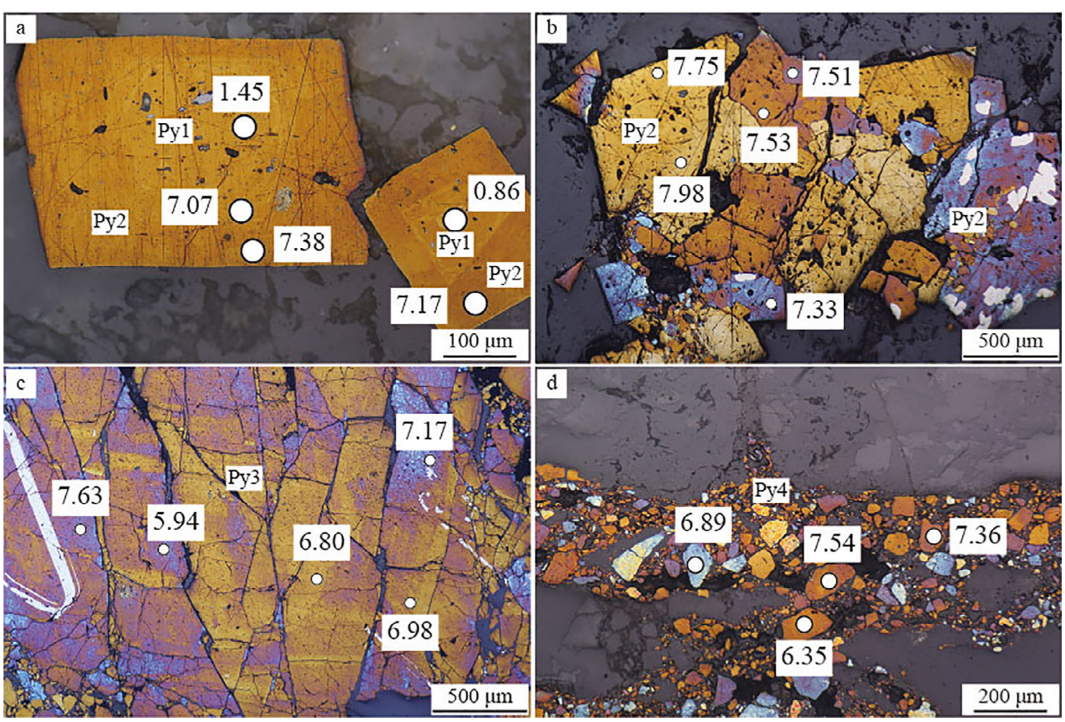


**Fig. 10.** Analysis spots of pyrite and $\delta^{34}S$ values. (a) Distinct $\delta^{34}S$ value in single pyrite. (b–d) Py2, Py3, and Py4 have similar $\delta^{34}S$ values.

2009; Deol et al., 2012;). In the Jiangshan gold deposit, visible gold comprises mainly native gold (Fig. 11a and 11b) and electrum (Fig. 11c and 11d) and is generally less than 10 µm in diameter. Visible gold formed in Stage IV and occurs as inclusions and fracture-filled gold coexisting with Py4. Inclusion gold with round and elliptical shapes occur in Py4, quartz (Fig. 11b), or chalcopyrite (Fig. 11c). Fracture-filling gold occurs in pyrite fractures and has elongated shapes (Fig. 11a, 11b, and 11d). Invisible gold has two forms in pyrite, namely nanoparticles and solid solution. The LA-ICP-MS spot analyses of the pyrite plot below the gold saturation line in Fig. 8a confirmed that gold

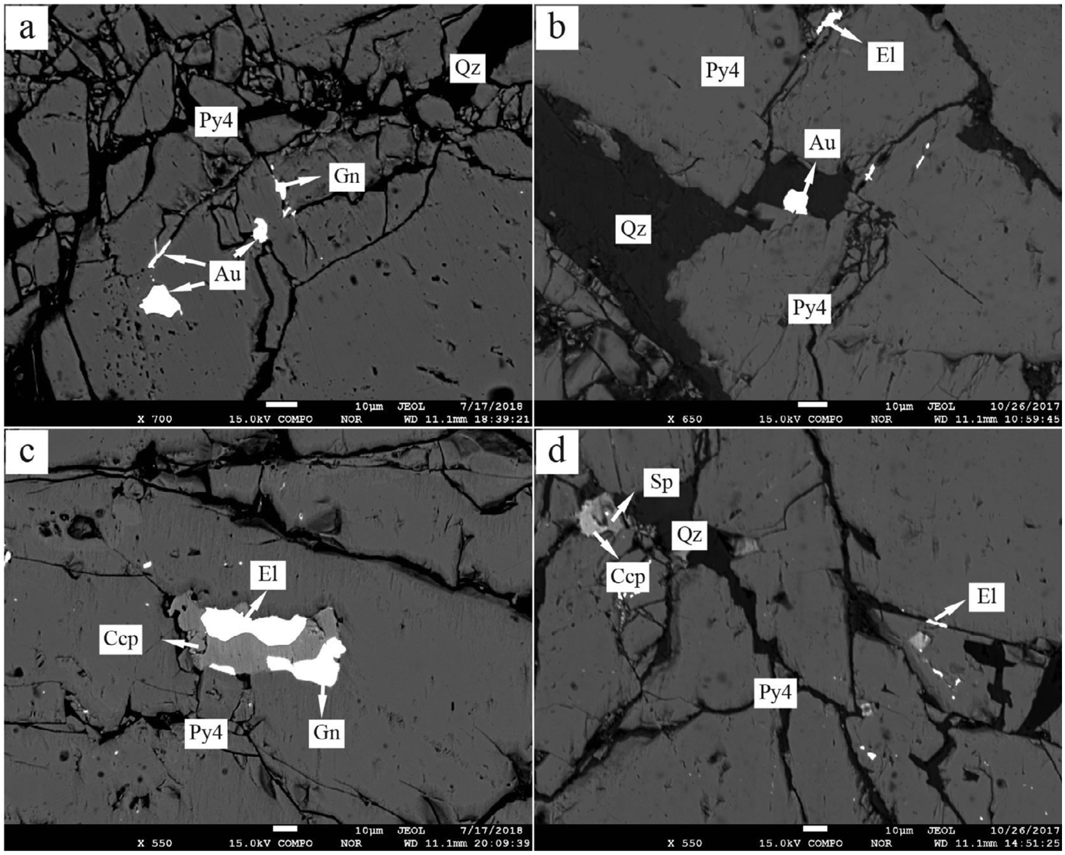


**Fig. 11.** Distribution of gold and electrum. (a) Py4 with native gold and microfractures filled with native gold and galena. (b) Native gold occurs in boundary of Py4 and quartz, and electrum fills microfractures. (c) Electrum and galena in boundary between Py4 and chalcopyrite. (d) Electrum, chalcopyrite, and sphalerite in microfractures. Au-native gold; El-electrum; Ccp-chalcopyrite; Gn-galena; Sp- sphalerite.

in pyrite occurs mostly in solid solution. Only one Py4 plotted above the gold saturation line (Fig. 8a), showing that little gold is present as nanoparticles in Py4.

In Jiangshan deposit, gold is mainly present in solid solution in pyrite, with little gold occurring as native gold or nanoparticles. Considering the hydrothermal pyrite in this deposit, the gold content in Py2 is slightly lower than that of Py3, but both are much lower than that of Py4 (Fig. 9a). Pyrite mapping indicated gold enrichment in Py4 (Fig. 12), and native gold and electrum formed in Stage IV. Stage IV is believed to be the main gold mineralization stage. Py4 is also enriched with chalcophile elements, such as copper, silver, arsenic, antimony, and lead.

### 6.2. Process of gold mineralization

Elliptical and irregularly shaped Py1 formed in the pre-ore stage (Fig. 13a). Py2, with euhedral and subhedral crystals, formed in Stage II disseminated and as clusters in pyrite–quartz–muscovite-altered rock with a small amount of carbonate (Fig. 5e and 5f). The pyrite–quartz–muscovite alteration zone developed along the footwall fault (Fig. 3b), and it is considered to be the channel for fluid migration. Moreover, fault activity may induce fluid movement. Some Py2 has a core of Py1, and the boundaries show irregular shapes and corrosion textures. Based on the mineral assemblages and pyrite textures in Py1 and Py2, the fluid in Stage II may have interacted with the host rocks. NaOCl etching of Py2 showed that some pyrites have rhythmic zoning caused by changes in cobalt and nickel contents (Fig. 6). Rhythmic zones in pyrite have been documented in numerous gold deposits, where they were attributed to the pyrite growth rate or addition of multiple hydrothermal fluids (Barker et al., 2009; Barker and Cox, 2011; Fougerouse et al., 2016). Variations in fluid composition from multiple hydrothermal events usually cause different stages of sulfides with irregular boundaries, corrosion textures, and distinct sulfur isotope (Barker et al., 2009; Peterson and Mavrogenes, 2014). However, these features are inconsistent with what we observe in Py2. Therefore, we conclude that the trace element zones in Py2 may have been produced by changes in the pyrite growth rate. The gold content in Py2 is low, and 90% of the data are less than 0.5 ppm (Fig. 9a, Table 2), indicating that Stage II is not the major mineralization stage in Jiangshan deposit (Fig. 13b).

Peterson and Mavrogenes (2014) mentioned that when fluid pressure is high, fluids permeate and react with the wall works until the rock fails. On failure, fluids that had penetrated the wallrocks will be driven back into the conduit, and a surge of fluid from the underlying source will be added to the system. In Jiangshan deposit, at the initial stage of mineralization, fluid permeated and reacted with wall rocks, causing the rock to break. This increased fluid flow from the underlying source and transport along the fault, forming pyrite–quartz veins. Py3 in pyrite–quartz veins has planar and anhedral crystals with many fractures (Fig. 7a). In contrast to Py2, Py3 has no Py1 or Py2 cores. This stage also has no altered minerals and only forms pyrite and quartz. This may be caused by direct precipitation of pyrite and quartz from hydrothermal fluids (Fig. 13c). The gold content in Py3 is higher than that in Py2, but the data are mostly lower than 1 ppm, indicating that this is not the major mineralization stage.

Py4 in quartz–pyrite veinlets with cataclastic textures and irregular shapes crosscuts the other three pyrite types (Fig. 7a and c). The quartz in stage IV also has cataclastic textures (Fig. 7d). The occurrence of cataclastic textures in both stage IV pyrite (Py4) and quartz indicates its formation was associated with a tectonic event. Both Py2 and Py3 have

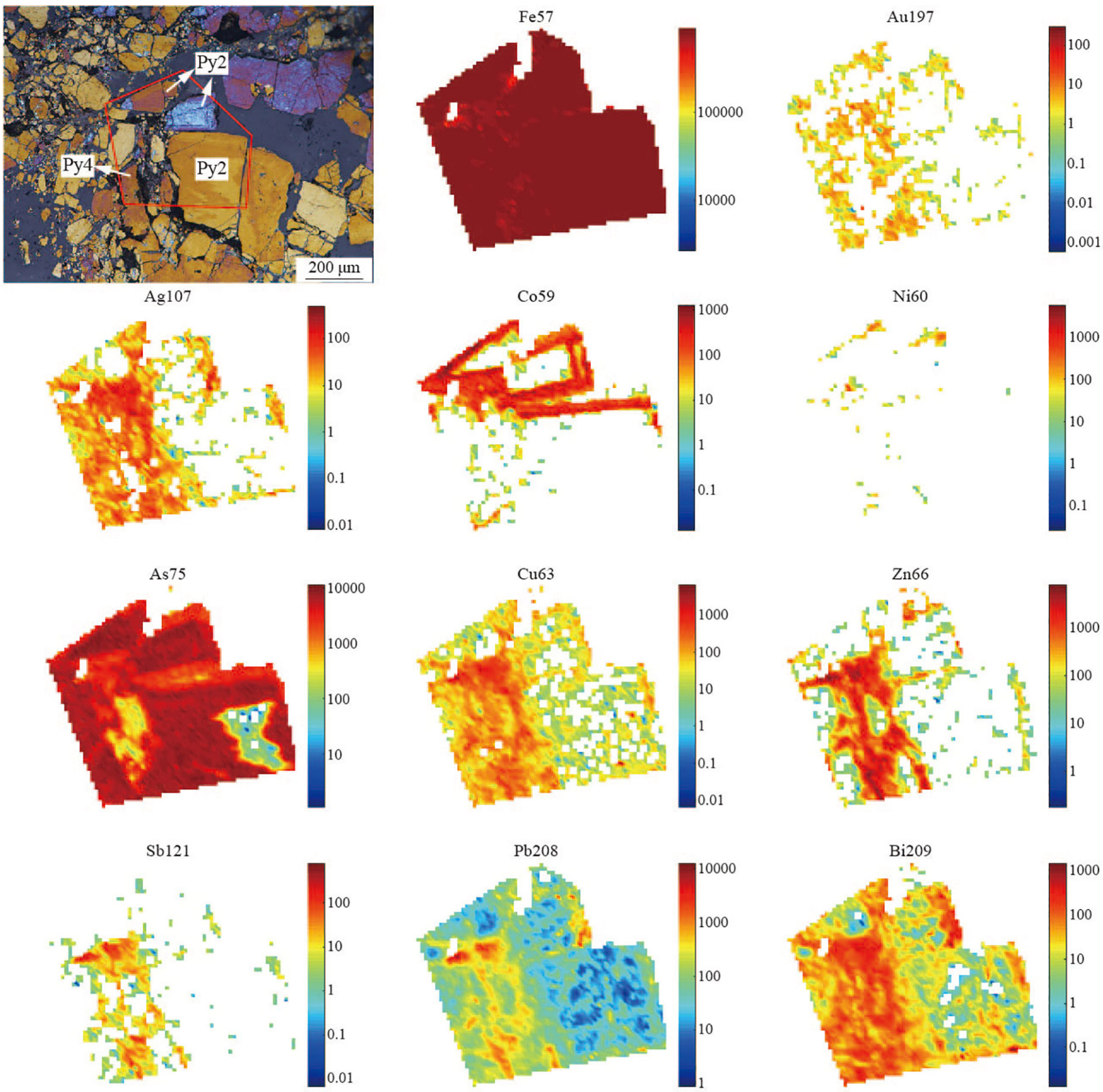


**Fig. 12.** Laser ablation inductively coupled plasma mass spectrometry images with logarithmic color scales (in ppm) showing trace element contents of Py2 and Py4.

many fractures and cataclastic textures showing they also experienced strong brittle deformation (Fig. 5d, 7a, and c), which shows that there was a tectonic deformation event after the formation of Py2 and Py3. We infer that the tectonic event caused a sudden drop in pressure and rapid pyrite crystallization and precipitation to form Py4, which has a cataclastic texture indicating that deformation continued after deposition. This decrease in pressure triggered phase separation, during which the exsolution of volatiles changed the fluid chemistry to induce gold precipitation (Sibson et al., 1988; Loucks and Mavrogenes, 1999; Peterson and Mavrogenes, 2014; Velasquez et al., 2014). The gold content in Py4 is the highest observed at Jiangshan, and most analyses are > 1 ppm, with some reaching 20 ppm. Stage IV is considered the major mineralization stage, and the associated tectonic event was the main controlling factor for gold mineralization in Jiangshan deposit (Fig. 13d).

### 6.3. Sulfur source

Py1 grains have the lowest $\delta^{34}S$ value (0.86–2.86‰), with a mean of 1.89‰which is considered to be pre-ore stage pyrite. Hematite and sulfate are not found in the Jiangshan gold deposit, and the sulfides are dominated by pyrite, with little chalcopyrite and galena. Isotopic fractionation between sulfide pairs is thus negligible. The sulfur isotope signature in the hydrothermal stage pyrite can reasonably represent the sulfur isotope composition of the fluid. The narrow range (5.79–7.89‰) and similarities of the sulfur isotope compositions between Py2, Py3, and Py4 suggest that the different stages of hydrothermal fluids were derived from a same reservoir (Fig. 14). Previous studies have shown that the sulfur isotopes of hydrothermal sulfides are strongly affected by temperature, pH, oxygen fugacity, and parental fluid composition, but changes due to pressure are minimal (Ohmoto, 1972; Seal, 2006). The tectonic event caused a rapid drop in pressure and induced gold precipitation (Peterson and Mavrogenes, 2014; Velasquez et al., 2014). The main factor in gold precipitation was the decreasing pressure from Stage II to IV; thus the sulfur isotopic ratio in hydrothermal pyrite did not change.

The quartz D–O in other gold deposits in the Bengbu Uplift ranged from −58 to −90‰ (δD) and 11.6 to 14.6‰ ($\delta^{18}O$), suggesting that

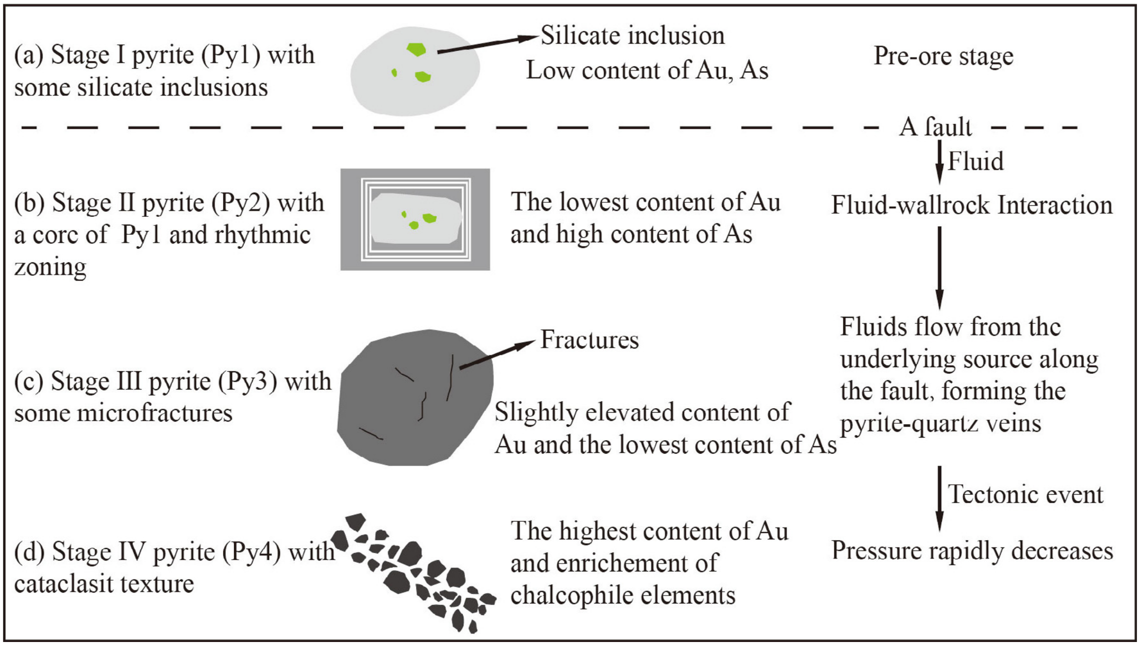


**Fig. 13.** Schematic diagram of different types of pyrite in Jiangshan gold deposit.

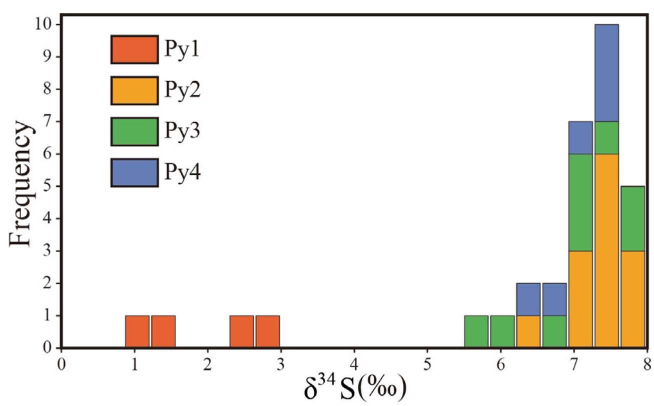


**Fig. 14.** Histogram of in-situ (SHRIMP) sulfur isotope compositions for four types of pyrite.

the ore-forming fluids were derived from mantle-derived magmatic fluids mixed with meteoric water (Wei, 2011; Liu, 2014; Yang et al., 2019). Previous researchers used He–Ar isotopes and C isotopes from early Cretaceous gold deposits in the NCC to show that ore-forming fluids were predominantly derived from the mantle (Li et al., 2012a,b; Zhu et al. 2015; Feng et al., 2019; Liu et al., 2019; Yuan et al., 2019; Deng et al., 2020). Therefore, we speculate that the hydrothermal fluids of Jiangshan deposit were mainly exsolved from mantle-derived magmas. The $\delta^{34}S$ values of Py2–Py4 are higher than those of chondrite ($\delta^{34}S = 0 \pm 3‰$) (Chaussidon and Lorand, 1990). The metamorphic rocks in the Bengbu Uplift had sulfur isotope values of 2‰ (Wei, 2011), with no evaporites. Even if the sulfur in the strata were incorporated into ore-forming fluids, it would have been impossible for the sulfur isotope values in the fluids to reach 5–8‰.

The $\delta^{34}S$ values in Jiangshan deposit were mainly controlled by the sulfur isotopic composition of the parental fluids. The high $\delta^{34}S$ values indicate that the ore-forming fluids were related to degassing of the mantle wedge metasomatized by slab fluids (Cai et al., 2018). Chen et al. (2018) used the age of dikes in Jiangshan deposit to limit the time of mineralization to 121–128 Ma. Previous studies suggested that during the westward subduction of the palaeo-Pacific plate in the early Cretaceous, parts of the subducted slab became stagnant in the mantle transition zone under the eastern NCC, leading to intense metasomatism of the lithospheric mantle and increased oxygen fugacity (Zhu et al., 2015; Cai et al., 2018). This process could have resulted in the enrichment of $^{34}S$ (Ionov et al., 1992). Fluids released from the stalled subduction plate and overlying oceanic sediments have also been suggested as important carriers of gold and S (Large et al., 2014; Goldfarb and Santosh, 2014; Groves and Santosh, 2016). Because $H_2S$ is generally rich in $^{32}S$, $H_2S$ degassing of mantle-derived magma probably increased the $^{34}S$ in residual magma and formed $^{34}S$-rich magmatic fluids from which $S^{34}$-enriched pyrite ($\delta^{34}S = 5–8‰$) could precipitate.

### *6.4. Implication for fracture-disseminated type gold deposit*

Li et al. (2012a,b, 2015) concluded that low angle faults (< 45°) control the formation of fracture-disseminated-type gold deposits. Fluids migrate along the fault and react with the wall rocks to generate broad zones of alteration accompanied by gold beneath the fault. The ore bodies in Jiangshan deposit are mainly located in the fault footwall and are structurally controlled by the fault. The ore is dominated by pyrite–quartz–muscovite-altered rocks and quartz–pyrite veinlets. These characteristics are similar to those of the fracture-disseminated-type gold deposit (Jiaojia-type) in Jiaodong district (Li et al., 2015; Yang et al., 2016a; Yang and Santosh, 2020). Moreover, the sulfur isotopes of pyrite in the Jiaojia-type gold deposit have $\delta S^{34}$ between 4 and 11‰ (Deng et al., 2015; Wen et al., 2015; Yang et al., 2016b; Ma et al., 2018; Deng et al., 2020). This is consistent with the sulfur isotopes of pyrite in Jiangshan deposit, supporting its classification as a fracture-disseminated-type gold deposit.

This study of trace elements in different types of pyrite in Jiangshan gold deposit showed that pyrite formed during the tectonic event has the highest gold concentration. The fault was not only the migration channel for hydrothermal fluids, but the tectonic event was also responsible for enrichment and precipitation of gold, making it the most important factor in producing fracture-disseminated type gold deposits.

## 7. Conclusions

The following conclusions were drawn from this study:

(1) Jiangshan gold deposit comprised four stages: pre-ore stage (stage

I), pyrite–quartz–muscovite alteration stage (stage II), pyrite–quartz vein stage (Stage III), and quartz–pyrite veinlet stage (Stage IV). Py1, Py2, Py3, and Py4 formed in these four stages, respectively.

(2) Of the pyrite types, Py4 has the highest gold concentration, associated with native gold and electrum formed during Stage IV. Thus this stage was the main mineralization stage, during which enrichment and precipitation of gold were strongly affected by the associated tectonic event.

(3) The mean $\delta^{34}S$ sulfur isotopic value of pre-ore stage pyrite is 1.89‰. The narrow range (5.79–7.98‰) in the hydrothermal pyrite indicates that hydrothermal fluids were related to degassing of the mantle wedge metasomatized by slab fluids.

(4) By analogy with similar deposits in Jiaodong gold province, Jiangshan gold deposit is considered to be a fracture-disseminated-type gold deposit. Mineralization is closely associated, both spatially and temporally, with a tectonic event that is probably the dominant factor in producing this type of gold deposit.

## Declaration of Competing Interest

The authors declare that they have no known competing financial interests or personal relationships that could have appeared to influence the work reported in this paper.

## Acknowledgements

This work was financially supported by the National Key Research and Development Plan (grant No. 2016YFC0600206), the National Natural Science Foundation of China (grant No. 41672081), and the Public Welfare Project of Anhui Province (grant No. 2016-g-3-35). We are grateful to geologists from No. 312 Unit of Bureau of Geology and Mineral Exploration of Anhui Province for their field assistance. We also thanks to Fangyue Wang for his help during the LA-ICP-MS analyses.

## References

Barker, S.L., Cox, S.F., 2011. Oscillatory zoning and trace element incorporation in hydrothermal minerals: insights from calcite growth experiments. Geofluids 11, 48–56.
Barker, S.L., Hickey, K.A., Cline, J.S., Dipple, G.M., Kilburn, M.R., Vaughan, J.R., Longo, A.S., 2009. Uncloaking invisible gold: use of Nanosims to evaluate gold, trace elements, and sulfur isotopes in pyrite from Carlin-type gold deposits. Econ. Geol. 107, 897–904.
Cai, Y.C., Fan, H.R., Santosh, M., Hu, F.F., Yang, K.F., Li, X.H., 2018. Decratonic gold mineralization: Evidence from the Shangzhuang gold deposit, eastern North China Craton. Gondwana Res. 54, 1–22.
Chaussidon, M., Lorand, J.P., 1990. Sulfur isotope composition of spinel lherzolite massifs from Ariege (North-Eastern Pyrenees, France): An ion microprobe study. Geochim. Cosmochim. Acta 54, 2835–2846.
Chen, Y., Fan, Y., Liu, Q., Li, C.W., Huang, Y., Chen, X., Wang, B., Liu, Y.N., 2018. Zircon chronology of ore-bearing strata and related magmatic rocks in Jiangshan gold deposit, Fengyang, Anhui Province, and its significance. Mineral Deposits 37 (6), 1217–1236 (in Chinese with English abstract).
Cook, N.J., Ciobanu, C.L., Mao, J.W., 2009. Textural control on gold distribution in As-free pyrite from the Dongping, Huangtuliang and Hougou gold deposits, North China Craton (Hebei Province, China). Chem. Geol. 264, 101–121.
Crow, D., Waughan, R., 1966. Characterization and use of isotopically homogeneous standards for in situ laser microprobe analysis of 34S/32S rations. Am. Mineral. 81, 187–193.
Deng, J., Liu, X.F., Wang, Q.F., Pan, R.G., 2015. Origin of the Jiaodong-type Xinli gold deposit, Jiaodong Peninsula, China: Constrains from fluid inclusion and C-D-O-S-Sr isotope compositions. Ore Geol. Rev. 65, 674–686.
Deng, J., Wang, Q.F., 2016. Gold mineralization in China: Metallogenic provinces, deposit types and tectonic framework. Gondwana Res. 36, 219–274.
Deng, J., Wang, C.M., Bagas, L., Santosh, M., Yao, E.Y., 2018. Crustal architecture and metallogenesis in the south-eastern North China Craton. Earth-Sci. Rev. 182, 251–272.
Deng, J., Wang, Q.F., Santosh, M., Liu, X.F., Liang, Y.Y., Yang, L.Q., Zhao, R., Yang, L., 2020. Remobilization of metasomatized mantle lithosphere: a new model for the Jiaodong gold province, eastern China. Mineral Deposits. 55, 257–274.
Deol, S., Large, R.R., Gilbert, S., 2012. LA-ICPMS and EPMA studies of pyrite, arsenopyrite and loellingite from the Bhukia-Jagpura gold prospect, southern Rajasthan, India: Implications for ore genesis and gold remobilization. Chem. Geol. 326–327, 72–87.
Feng, K., Fan, H.R., Groves, D.I., Yang, K.F., Hu, F.F., Liu, X., Cai, Y.C., 2019. Geochronological and sulfur isotopic evidence for the genesis of the post-magmatic, deeply sources, and anomalously gold-rich Daliuhang orogenic deposit, Jiaodong, China. Mineral Deposits. https://doi.org/10.1007/s00126-019-00882-8.
Fougerouse, D., Micklethwaite, S., Tomkins, A.G., Mei, Y., Kilburn, M., Guagliardo, P., Fisher, L.A., Halfpenny, A., Gee, M., Paterson, D., Howard, D.L., 2016. Gold remobilisation and formation of high grade ore shoots driven by dissolution-reprecipitation replacement and Ni substitution into auriferous arsenopyrite. Geochim. Cosmochim. Acta. 178, 143–159.
Goldfarb J., R, Santosh, M., 2014. The dilemma of the Jiaodong gold deposits: are they unique? Geosci. Front 5, 139–153.
Goldgarb, R.J., Groves, D.I., 2015. Orogenic gold: Common or evolving fluid and metal sources and through time. Lithosphere 233, 2–26.
Groves, D.I., Santosh, M., 2016. The giant Jiaodong gold province: The key to a unified model for orogenic gold deposit. Geosci. Front. 7, 409–417.
Groves, D.I., Santosh, M., Deng, Jun, Wang, Q.F., Yang, L.Q., Zhang, L., 2020. A holistic model for the origin of orogenic gold deposits and its implications for exploration. Mineral. Petrol. 55, 275–292.
Guo, S.S., Li, S.G., 2009a. SHRIMP zircon U-Pb ages for the Paleoproterozoic metamorphic-magmatic events in the southeast margin of the North China Craton. Sci. China Ser. D Earth Sci. 52 (8), 1039–1045.
Guo, S.S., Li, S.G., 2009b. Petrochemical characteristics of leucogranite and a case study of Bengbu leucogranites. Sci. China Ser. D Earth Sci. 54, 1923–1930.
Hou, L., Peng, H.J., Ding, J., Zhang, J.R., Zhu, S.B., Wu, S.Y., Wu, Y., Ouyang, H.G., 2016. Textures and in situ chemical and isotopic analyses of pyrite, Huijiabao Trend, Youjiang Basin, China: Implications for paragenesis and source of sulfur. Econ. Geol. 111, 331–353.
Hu, H.F., Xu, X.C., Chen, F., Xu, W., 2015. A comparison of metallogenetic geological condition of gold deposits between the Bengbu-Wuhe area in Anhui and Eastern Shandong Province. J. Geol. 39, 187–193 (in Chinese with English abstract).
Ionov, D.A., Hoefs, J., Wedepohl, K.H., Wiechert, W., 1992. Content and isotopic composition of sulphur in ultramafic xenoliths from central Asia. Earth Planet. Sci. Lett. 111, 269–286.
Ireland, T.R., Schram, N., Holden, P., Lanc, P., Ávila, J., Armstrong, R., Amelin, Y., Latimore, A., Corrigan, D., Clement, S., Foster, J.J., Compston, W., 2014. Charge-mode electrometer measurements of S-isotopic compositions on SHRIMP-SI. Int. J. Mass Spectrom. 359, 26–37.
Kang, C.X., Yang, X.Z., Cai, Y.T., Zong, W., Huang, X.J., Kong, G.L., Li, C.W., 2018. Origin and dynamic background of Late Early Cretaceous monzonite granite in the Bengbu uplift, southeastern margin of the North China Craton. Acta Geol Sin. 92, 587–703 (in Chinese with English abstract).
Large, R.R., Halpin, J.A., Danyushevsky, L.V., Maslennikov, V.V., Bull, S.W., Long, J.A., Gregory, D.D., Lounejeva, E., Lyons, T.W., Sack, P.J., 2014. Trace element content of sedimentary pyrite as a new proxy for deep-time ocean-atmosphere evolution. Earth Planet. Sci. Lett. 389, 209–220.
Large, R.R., Danyushevsky, L., Maslennikov, V., Meffre, S., Gilbert, S., Bull, S., Scott, R., Emsbo, P., Thomas, H., Singh, B., Foster, J., 2009. Gold and trace element zonation in pyrite using a Laser Imaging Technique: Implications for the timing of gold in orogenic and Carlin-Style sediment-hosting deposits. Econ. Geol. 104, 635–668.
Large, R.R., Maslennikov, V., Robert, F., Danyushevsky, L., Chang, Z.S., 2007. Multistage sedimentary and metamorphic origin of pyrite and gold in the giant Sukhoi Log deposit, Lena gold province. Russia. Econ. Geol. 102, 1232–1267.
Leech, M.L., Webb, L.E., 2013. Is the UP-UHP Hong'an-Dabie-Sulu orogeny a piercing point for offset on the Tan-Lu fault? J. Asian Earth Sci. 63, 112–129.
Li, J., Li, Z., Zhou, M., 2012a. The Early Cretaceous Yangzhaiyu lode gold deposit, North China Craton: a link between craton reactivation and gold veining. Econ. Geol. 107, 43–79.
Li, J.W., Bi, S.J., Selby, D., Chen, L., Vasconcelos, P., Thiede, D., Zhou, M.F., Zhao, X.F., Li, Z.K., Qiu, H.N., 2012b. Giant Mesozoic gold province related to the destruction of North China Craton. Earth Planet. Sci. Lett. 349–350, 26–37.
Li, L., Santosh, M., 2014. The "Jiaodong type" gold deposits: characteristics, origin and prospecting. Ore Geol Rev. 65, 589e611.
Li, L., Santosh, M., Li, S.R., 2015. The "Jiaodong type" gold deposits: Characteristics, origin and prospecting. Ore Geol. Rev. 65, 589–611.
Li, S.G., Wang, S.J., Guo, S.S., Xiao, Y.L., Liu, S.A., He, Y.S., Liu, J.L., 2014. Geochronology and geochemistry of leucogranites from the southeast margin of the North China Block: Origin and migration. Gondwana Res. 26, 1111–1128.
Li, X.H., Fan, H.R., Yang, K.F., Hollings, P., Liu, X., Hu, F.F., Cai, Y.C., 2018. Pyrite textures and compositions from the Zhuangzi Au deposit, southeastern North China. Miner. Contrib. Mineral. Petrol. 173, 73.
Liu, J., Zhang, L.J., Wang, S.L., Li, T.G., Yang, Y., Liu, F.X., Li, S.H., Duan, C., 2019. Formation of the Wulong gold deposit, Liaodong gold province, NE China: Constraints from zircon U-Pb age, sericite Ar-Ar age, and H-O-S-He isotopes. Ore Geol. Rev. 109, 130–143.
Liu, Q., 2014. Geochemical tracing analysis of ore-forming material of gold polymetallic ore deposit in the Wuhe-Fengyan area. Geol. Anhui 24, 17–22 (in Chinese with English abstract).
Liu, S.A., Li, S.G., Guo, S.S., Hou, Z.H., He, Y.S., 2012a. The Cretaceous adakitic-basaltic-granitic magma sequence on south-eastern margin of the North China Craton: Implications for lithospheric thinning mechanism. Lithos. 134–135, 163–178.
Liu, Y.C., Wang, W.D., Rolfo, F., Groppo, C., Gu, X.F., Song, B., 2012b. Geochronological and petrological constraints on Palaeoproterozoic granulite facies metamorphism in southeastern margin of the North China Craton. J. Metamorph. Geol. 27, 125–138.
Liu, Y.S., Hu, Z.C., Gao, S., Gunther, D., Xu, J., Gao, C.G., Chen, H.H., 2008. In situ analysis of major and trace elements of anhydrous minerals by LA-ICP-MS without applying an internal standard. Chem. Geol. 257, 34–43.

Loucks, R.R., Mavrogenes, J.A., 1999. Gold solubility in supercritical hydrothermal brines measured in synthetic fluid inclusions. Science 284, 2159–2163.
Ma, W.D., Fan, H.R., Liu, X., Yang, K.F., Hu, F.F., Zhao, K.D., Cai, Y.C., Hu, H.L., 2018. Hydrothermal fluid evolution of the Jintingling gold deposit in the Jiaodong Peninsula, China: Constraints from U-Pb age, CL imaging, fluid inclusion and stable isotope. Ore Geol. Rev. 160, 287–303.
Ning, S.Y., Wang, F.Y., Xue, W.D., Zhou, T.F., 2017. Geochemistry of the Baoshan pluton in the Tongling region of the Lower Yangtze River Belt. Geochimica 46, 397–412 (in Chinese with English abstract).
Ohmoto, H., 1972. Systematics of sulfur and carbon isotopes in hydrothermal ore deposits. Econ. Geol. 67, 551–578.
Peterson, E.C., Mavrogenes, J.A., 2014. Linking high-grade gold mineralization to earthquake-induced fault-valve processes in the Porgera gold deposit, Papua New Guinea. Geology 42, 383–386.
Reich, M., Kesler, S.E., Utsunomiya, S., Palenik, C.S., Chryssoulis, S.L., Ewing, R.C., 2005. Solubility of gold in arsenian pyrite. Geochim. Cosmochim. Acta 69, 2781–2796.
Seal, R.R., 2006. Sulfur isotope geochemistry of sulfide minerals. Rev Mineral Geochem. 61, 633–677.
Sibson, R.H., Howard, F., Poulsen, K.H., 1988. High-angle reverse faults, fluid-pressure cycling, and mesothermal gold-quartz deposit. Geology 16, 551–555.
Velasquez, G., Beziat, D., Salvi, S., Siebenaller, L., Borisova, A.Y., Pokrovski, G.S., Parseval, P.D., 2014. Formation and deformation of pyrite and implications for gold mineralization in the El Callao District, Venezuela. Econ. Geol. 109, 457–486.
Wang, F.Y., Ge, C., Ning, S.Y., Zhong, G.X., White, N.C., 2017. A new approach to LA-ICP-MS mapping and application in geology. Acta Petrol. Sin. 33, 3422–3436 (in Chinese with English abstract).
Wang, Y., 2006. The onset of the Tan-Lu fault movement in eastern China: constraints from zircon (SHRIMP) and 40Ar/39Ar dating. Terra Nova. 18, 423–431.
Ward, J., Mavrogenes, J., Murray, A., Holden, P., 2017. Trace element and sulfur isotopic evidence for redox changes during formation of the Wallaby gold deposit, Western Australia. Ore Geol. Rev. 82, 31–48.
Wei, B., 2011. The study of mineralization and genesis of Au-Pb-Zn polymetallic deposit in Bengbu area of Anhui. China University of Geoscience, Beijing (Master Thesis).
Wen, B.J., Fan, H.R., Santosh, M., Hu, F.F., Pirajno, F., Yang, K.F., 2015. Genesis of two different types of gold mineralization in the Lingling gold field, China: Constrains from geology, fluid inclusions and stable isotope. Ore Geol. Rev. 65, 643–658.
Wu, F., Xiao, Y.L., Xu, L.J., Santosh, M., Li, S.G., Huang, J., Hou, Z.H., Huang, F., 2015. Geochronology and geochemistry of felsic xenoliths in lamprophyre dikes from the southeastern margin of the North China Craton: implications for the interleaving of the Dabie-Sulu orogenic crust. Int. Geol. Rev. 57, 1305–1325.
Xiong, S.F., Jiang, S.Y., Zhao, K.D., Ma, Y., Chen, Q.Z., Jiang, M.R., 2019. Gold distribution and source of the J4 gold-bearing breccia pipe in the Qiyugou district, North China Craton: Constraints from ore mineralogy and in situ analysis of trace elements and S-Pb isotopes. Ore Geol. Rev. 105, 514–536.
Xu, J.W., Zhu, G., Tong, W.X., Cui, K.R., Liu, Q., 1987. Formation and evolution of the Tancheng-Lujiang wrench fault system: a major shear system to the northwest of the Pacific Ocean. Tectonophysics 134, 273–310.
Xu, W.L., Wang, Q.H., Yang, D.B., Liu, X.C., Guo, J.H., 2005. SHRIMP zircon U-Pb dating in Jingshan “migmatitic granite”, Bengbu and its geological significance. Sci. China Ser. D Earth Sci. 48, 185–191.
Yang, C.X., Santosh, M., 2020. Ancient deep roots for Mesozoic world-class gold deposits in the north China craton: An integrated genetic perspective. Geosci. Front. 11, 203–214.
Yang, D.B., Xu, W.L., Pei, F.P., Wang, Q.H., Liu, X.M., 2005. Formation time and magma source of granites in Bengbu uplift, Evidence from LA-ICPMS zircon U-Pb dating and tracing. Geochimica 34, 443–454 (in Chinese with English abstract).
Yang, D.B., Xu, W.L., Wang, Q.H., Pei, F.P., 2010. Chronology and geochemistry of Mesozoic granitoids in the Bengbu area, central China: Constraints on the tectonic evolution of the eastern North China Craton. Lithos. 114, 200–216.
Yang, K.F., Jiang, P., Fan, H.R., Zuo, Y.B., Yang, Y.H., 2018. Tectonic transition from a compressional to extensional metallogenic environment at ~120 Ma revealed in the Hushan gold deposit, Jiaodong, North China Craton. J. Asian Earth Sci. 160, 408–425.
Yang, L.Q., Deng, J., Wang, Z.L., Guo, L.N., Li, R.H., Groves, D.I., Danyushevsky, L.V., Zhang, C., Zheng, X.L., Zhao, H., 2016a. Relationships between gold and pyrite at the Xincheng gold deposit, Jiaodong Peninsula, China: Implications for gold source and deposition in a brittle epizonal environment. Econ. Geol. 111, 105–126.
Yang, L.Q., Deng, J., Guo, L.N., Wang, Z.L., Li, X.Z., Li, J.L., 2016b. Origin and evolution of ore fluid, and gold-deposition processes at the giant Taishang gold deposit, Jiaodong Peninsula, eastern China. Ore Geol. Rev. 72, 585–602.
Yang, L.Q., Deng, J., Wang, Z.L., Guo, L.N., Song, M.C., Zheng, X.L., 2014. Mesozoic gold metallogenic system of the Jiaodong gold province, eastern China. Acta Petrol. Sin. 30, 2447–2467 (in Chinese with English abstract).
Yang, Q.Y., Santosh, M., 2015. Early Cretaceous magma flare-up and its implications on gold mineralization in the Jiaodong Peninsula. China. Ore Geol. Rev. 65, 626–642.
Yang, Z., Deng, Y.F., Yuan, F., Li, Y., Lin, T., Zhang, S.L., Zhang, J.J., 2019. Ore source and ore forming age of Hekou and Rongdu Au deposit in Wuhe area. Bengbu city. Acta Petrol. Sin. 35, 3875–3893 (in Chinese with English abstract).
Yuan, Z.Z., Li, Z.K., Zhao, X.F., Sun, H.S., Qiu, H.N., Li, J.W., 2019. New constraints on the genesis of the giant Dayingezhuang gold (silver) deposit in the Jiaodong district, North China Craton. Ore Geol. Rev. 112, 103038.
Zhai, M.G., Santosh, M., 2013. Metallogeny of the North China Craton: Link with secular changes in the evolving Earth. Gondwana Res. 24, 275–297.
Zhu, G., 1999. Discussion on the western extension of the Zhao-Ye gold ore belt, Shandong. Geol. Prospect. 35, 6–10 (in Chinese with English abstract).
Zhu, G., Wang, Y.S., Niu, M.L., Xie, C.L., Li, C.C., 2005. 40Ar/39Ar dating of strike-slip motion on the Tan-Lu fault zone, east China. J. Struct. Geol. 27, 1379–1398.
Zhu, R.X., Fan, H.R., Li, J.W., Meng, Q.R., Li, S.R., Zeng, Q.D., 2015. Decratonic gold deposits. Sci. China Ser. D Earth Sci. 58, 1523–1537.